

# Characterization of Residual Stresses in Friction Surfacing of Ti and Al Alloys

Dissertation with the aim of achieving a doctoral degree at the  
Faculty of Mathematics, Informatics and Natural Sciences  
Department of Physics Universität Hamburg

Submitted by Gleb Dovzhenko

2020 in Hamburg.

Gutachter/innen der Dissertation:

Prof. Dr. Andreas Schreyer

Prof. Dr. Martin Müller

Zusammensetzung der Prüfungskommission:

Prof. Dr. Andreas Schreyer

Prof. Dr. Martin Müller

Dr.-Ing. Stefanie Hanke

Prof. Dr. Florian Pyczak

Prof. Dr. Robin Santra

Vorsitzende/r der Prüfungskommission:

Prof. Dr. Robin Santra

Datum der Disputation:

05.02.2021

Vorsitzender Fach-Promotionsausschusses PHYSIK: Prof. Dr. Günter Hans Walter Sigl

Leiter der Fachbereichs PHYSIK:

Prof. Dr. Wolfgang Hansen

Dekan der Fakultät MIN:

Prof. Dr. Heinrich Graener

# Abstract

The investigation presented in this thesis is an overview of the relation between the Friction Surfacing deposition parameters and the residual stresses produced by the process. The investigation focuses on three coating / substrate combinations: Ti-6Al-4V on Ti-6Al-4V, AA6082 on AA2024, and AA5083 on AA2024. The residual stress distributions were obtained using non-destructive techniques: high energy X-ray and neutron diffraction. Additionally, thermal conditions during Friction Surfacing deposition were investigated with their connection to the residual stress state and the deposition efficiency.

The results reveal the connection between the deposition parameters such as the translational stud velocity and the post-deposition stress state. They show the effect of the stress state on the fatigue life of the samples, and the effect of post-deposition machining on the stress state. A theory connecting the thermal conditions during the deposition and the deposition efficiency is developed.

This investigation provides a first systematic outlook on the residual stresses produced by Friction Surfacing and allows to evaluate the process as a production tool for local strengthening and repair. The discovered connection between the deposition efficiency and the amount of heat dissipated from the depositing stud not only has practical applications for process control and design, but also invites to think about the process in more simple and fundamental terms.

# Kurzfassung

Die Untersuchung in der vorliegenden Dissertation ist eine Übersicht von Wechselwirkungen zwischen Auftragsparametern des Reibauftragschweißverfahrens und den bei diesem Prozess im Werkstück erzeugten Eigenspannungen. Diese Untersuchung ist auf die folgenden drei Kombinationen aus Auftrags- und Substratmaterial fokussiert: Ti-6Al-4V auf Ti-6Al-4V, AA6082 auf AA2024 und AA5083 auf AA2024. Die Eigenspannungsverteilungen erlangte man durch die Anwendung zerstörungsfreier Untersuchungstechniken wie hochenergetischer Röntgen- und Neutronendiffraktion. Zusätzlich wurden die thermischen Bedingungen im Reibauftragschweißverfahren untersucht und mit dem Eigenspannungszustand sowie mit der Auftragungseffizienz verknüpft.

Die Resultate decken die Verbindung zwischen den Auftragsparametern wie der horizontalen, translatorischen Vorschubgeschwindigkeit des Auftragsreibbolzens während des Schweißprozesses und dem Spannungszustand nach dem erfolgten Schweißprozess auf. Sie zeigen den Effekt des Spannungszustands auf die Lebensdauer der Schweißverbindung auf sowie den Einfluss einer spannenden Bearbeitung nach erfolgtem Schweißprozess, auf den im Werkstück herrschenden Spannungszustand. Dazu wurde eine Theorie entwickelt, die die thermischen Bedingungen während des Auftragsprozesses mit der Auftragungseffizienz des Reibbolzenmaterials auf das Substrat verknüpft.

Diese Untersuchung liefert eine erste systematische Vorhersage der durch das Reibauftragschweißverfahren erzeugten Eigenspannungen und erlaubt es so dieses Verfahren als Fertigungshilfsmittel für lokale Strukturverstärkungen und Strukturreparaturen zu evaluieren. Die Entdeckung der Verknüpfung zwischen der Materialauftragungseffizienz und der dissipierten Wärmemenge vom Auftragsreibbolzen hat nicht nur praktische Folgen für die Anwendung zur Verfahrensparametersteuerung und Design, sondern lädt auch dazu ein in mehr vereinheitlichter und fundamentaler Art den Prozess des Reibauftragschweißverfahrens zu betrachten.

# Eidesstattliche Versicherung / Declaration on oath

Hiermit versichere ich an Eides statt, die vorliegende Dissertationsschrift selbst verfasst und keine anderen als die angegebenen Hilfsmittel und Quellen benutzt zu haben. Die eingereichte schriftliche Fassung entspricht der auf dem elektronischen Speichermedium.

Die Dissertation wurde in der vorgelegten oder einer ähnlichen Form nicht schon einmal in einem früheren Promotionsverfahren angenommen oder als ungenügend beurteilt.

Hamburg, den 01.11.2020

A handwritten signature in black ink, reading "G. Douzhenko". The signature is written in a cursive style with a large initial "G" and a long, sweeping underline.

# List of publications

[Dovzhenko et al., 2018] Dovzhenko, G., Hanke, S., Staron, P., Maawad, E., Schreyer, A., and Horstmann, M. (2018). Residual stresses and fatigue crack growth in friction surfacing coated Ti-6Al-4V sheets. *Journal of Materials Processing Technology*, 262:104–110.

# Contents

<b>1</b>	<b>Introduction</b>	<b>10</b>
<b>2</b>	<b>The Friction Surfacing Process</b>	<b>13</b>
2.1	Friction Surfacing . . . . .	13
2.2	Residual stresses in welding processes . . . . .	18
<b>3</b>	<b>Experimental Techniques</b>	<b>21</b>
3.1	Diffraction techniques . . . . .	21
3.2	FCP Testing . . . . .	27
3.3	Temperature measurements during Friction Surfacing coating deposition	28
<b>4</b>	<b>Residual Stresses and Fatigue Crack Growth in Friction Surfacing Coated Ti-6Al-4V Sheets</b>	<b>29</b>
4.1	Introduction . . . . .	29
4.2	Materials and experimental procedure . . . . .	31
4.3	Results and discussion . . . . .	33
4.4	Conclusions . . . . .	45
<b>5</b>	<b>Residual Stresses in Friction Surfacing Coated AA2024 Sheets</b>	<b>46</b>

5.1	Introduction . . . . .	46
5.2	Materials and experimental procedure . . . . .	47
5.3	Results and discussion . . . . .	49
5.4	Conclusions . . . . .	57
<b>6</b>	<b>Deposition efficiency of Friction Surfacing on AA2024 Sheets</b>	<b>58</b>
6.1	Introduction . . . . .	58
6.2	Experimental and numerical procedure . . . . .	59
6.3	Results and discussion . . . . .	64
6.4	Conclusions . . . . .	73
<b>7</b>	<b>Overall results and discussion</b>	<b>75</b>
7.1	Residual stress characterization of Friction Surfacing . . . . .	75
7.2	On the deposition efficiency of Friction Surfacing . . . . .	79
7.3	On the scientific methods used in the study . . . . .	82
<b>8</b>	<b>Summary</b>	<b>83</b>

# List of Symbols and Abbreviations

**LN<sub>2</sub>** liquid nitrogen. 59, 64

**EDM** electrical discharge machining. 27, 48

**FCP** Fatigue Crack Propagation. 27, 29, 40, 43

**FEM** Finite Element Method. 12, 58, 66, 69, 79, 84

**FS** Friction Surfacing. 10–14, 16, 17, 23, 27–31, 34–36, 41, 45–47, 49, 52, 53, 55, 57–59, 62, 64, 69–73, 75–77, 79, 80, 83, 84

**FSC** Friction Stir Channeling. 10

**FSW** Friction Stir Welding. 10, 11, 30, 34–36, 41, 45

**HAZ** heat-affected zone. 31, 36, 74

**RS** residual stress. 11, 12, 19, 20, 29, 30, 34–37, 39–47, 49–58, 71–75, 77, 78, 82, 84

**TC** thermocouple. 28, 59, 61–63, 66–68

# Chapter 1

## Introduction

Friction Surfacing (FS) is a solid state deposition process, where a coating is generated from a metallic consumable stud. During the deposition the stud is rotating, and its flat end is pressed against the substrate surface with an axial loading force. The stud material plasticises from the frictional heating and shear forces acting in the rubbing interface and is deposited on the substrate surface as the rod moves across.

FS was first patented in United Kingdom by [Klopstock and Neelands, 1941], and its development later served as a basis for other friction-based techniques, such as Friction Stir Welding (FSW) or Friction Stir Channeling (FSC). Today FS is best known for enabling dissimilar material combinations that are impossible to join otherwise. FS weldable materials include various steels, Al- and Mg-based alloys, copper, Inconel, NiAl bronze and Ti-based alloys [Gandra et al., 2014].

Although FS offers limited control over deposit geometry, it is well suited for localised repair and cladding. According to [Vilaca et al., 2012] it has found multiple repair applications: the process has been used for rehabilitation of worn or damaged parts, such as turbine blade tips and agricultural machinery. In production FS has been used for buildup of long-life industrial blades, wear resistant components, and anti-corrosion coatings. Reported potential applications include reclamation of worn railway points and hermetic container sealing.

With applications in repair it is natural to make sure that the process does not reduce the quality of the part. One of the possible issues for welding processes is introducing

residual stresses that often cause problems either due to distortion or performance degradation [Withers and Bhadeshia, 2001]. While the residual stress state of FSW has been investigated for some materials ([Lombard et al., 2009] for AA5083, and [Romero et al., 2009] for Ti-6Al-4V), for FS at the moment there are no available publications, except by the author of this thesis [Dovzhenko et al., 2018]. The aim of this study is to fill this knowledge gap.

The investigation presented in this thesis is an overview of the relation between the FS process parameters and the residual stresses produced by the process. The investigation focuses on two materials that are deposited under different conditions: Ti deposition happens at high temperature and relatively low axial force ( $\sim 1300^\circ\text{C}$ ,  $2 - 3\text{ kN}$ ), and Al deposition at lower temperatures and higher axial forces ( $\sim 500^\circ\text{C}$ ,  $\sim 9\text{ kN}$ ). The goal of this study is to make a general overview over the creation of residual stresses in the process, from which further investigations of specific materials and conditions can progress.

The study is presented in Chapters 2 - 7. Chapter 2 introduces the reader to the FS process and to the fundamentals of residual stresses in welding. Chapter 3 presents the experimental techniques used in the study.

Chapter 4 presents a study of the relation between the translational stud speed during deposition and the final residual stress (RS) state for the FS of Ti-6Al-4V on 2 mm thick Ti-6Al-4V sheets. The RS state has been probed using monochromatic high-energy X-ray diffraction. Additionally, the mechanical properties of the coated sheets were tested by Fatigue Crack Propagation. The results of this study have been published [Dovzhenko et al., 2018] as a first investigation of the RS state of FS coated sheets.

Chapters 5 and 6 are an in-depth investigation of FS on Al alloys. Chapter 5, similar to Chapter 4, investigates the relation between the RS and translational stud speed during the FS deposition of AA6082 and AA5083 coatings on AA2024 substrates. In addition to the in-transmission stress measurements using X-ray diffraction, depth stress profiles were obtained using angle-dispersive neutron diffraction and X-ray diffraction with a conical slit cell. An important part of this study is the investigation of the effect machining has on the RS state of the FS coating, since machining

the coating would be necessary in production due to the coating's irregular shape.

Chapter 6 investigates the thermal conditions during the FS deposition of AA6082 on AA2024. Multiple depositions were performed at different temperature ranges, and the temperature data was then used in a Finite Element Method (FEM) model to estimate the heat input into the substrate for each deposition. This investigation provides an insight into the formation of the RS investigated in Chapter 5. Based on the same data and FEM model, the connection between heat dissipation and deposition efficiency was investigated for AA6082 on AA2024 FS welds. The results have shown that for AA6082 on AA2024 FS welds an increase of the heat dissipation from the depositing rod increases the amount of deposited material. This fundamental result has practical applications, revealing the necessity of a heat sink when depositing Al-based alloys on thin Al-based substrates, and gives a general insight into the process: at a certain parameter window the efficiency of FS deposition is a linear function of the amount of heat the setup is able to dissipate from the rod. At the time of submission of this thesis, the results of Chapter 6 are submitted for publication.

Finally, Chapter 7 combines the results of the previous chapters and presents an overview of achievements and future challenges. A short summary of the results and their context is presented in Chapter 8.

# Chapter 2

## The Friction Surfacing Process

### 2.1 Friction Surfacing

**Deposition Process** FS is a solid state deposition process, where a coating is generated from a metallic consumable rod [Gandra et al., 2014]. Stages of the deposition process can be seen on Fig. 2.1: the rod is rotating (a) and pressed against the substrate under an applied axial load (b). The rod tip gets hot and plastically deformed and a metallic bond forms due to diffusion between the plasticised rod material and the substrate surface (c). Part of the plasticised material forms a revolving flash at the rod tip, giving it a characteristic mushroom-shaped geometry. By applying a translational movement the plastic material gets deposited on the substrate in a continuous process (d). The process and the coatings produced by it are asymmetric: as the stud rotates and moves along the substrate surface, its advancing and retreating sides, where rotational movement is in the same or the opposite direction to the translational (back and front sides on Fig. 2.1 respectively) may display different behaviour [Gandra et al., 2014]. Examples of deposited Grade 1 Ti and AA6082 FS coatings can be seen on Figure 2.2.

**Microstructural properties** FS coatings present metallurgical characteristics typical for hot forging operations [Vilaca et al., 2012]. As the consumable rod material undergoes a thermo-mechanical process, a fine grained microstructure is produced by

dynamic recrystallization. An example of Ti-6Al-4V microstructure refinement from [Fitseva et al., 2016] can be seen on Fig. 2.3. Ti-6Al-4V FS deposits show refined microstructure in both coating and heat affected zone of the substrate. The AA6082 coatings investigated by [Gandra et al., 2013] on Fig. 2.4 show refined microstructure only in the coating with 33% mean grain size reduction compared to the initial state of the rod.

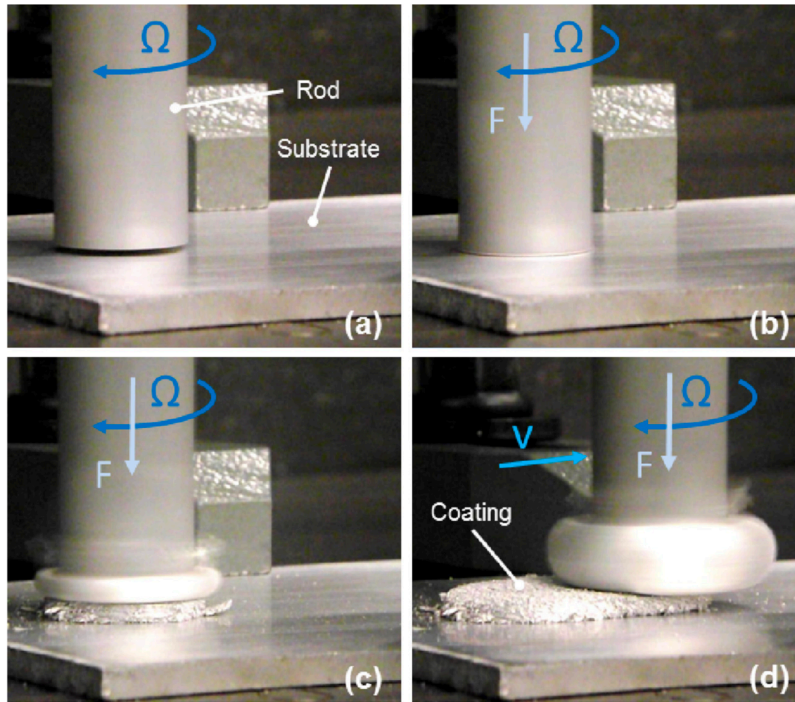


Figure 2.1: FS of an AA6082-T6 aluminium alloy over AA2024-T3, [Gandra et al., 2014]

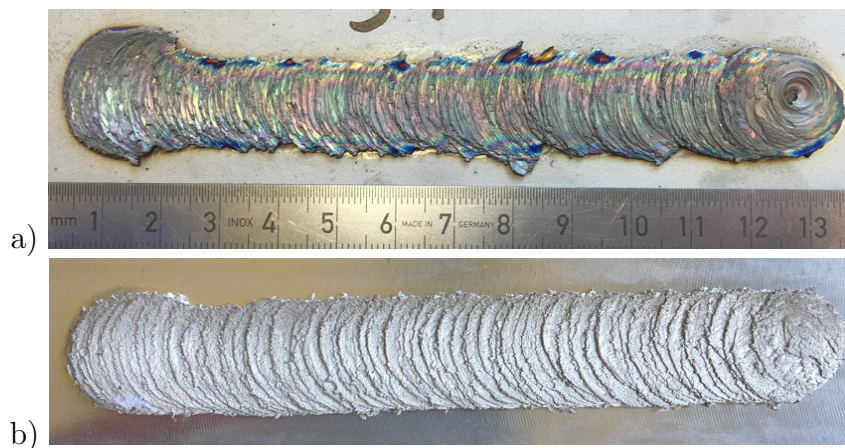


Figure 2.2: Typical FS coatings. a) Grade 1 Ti coating and substrate. b) AA6082 coating on AA2024 substrate.

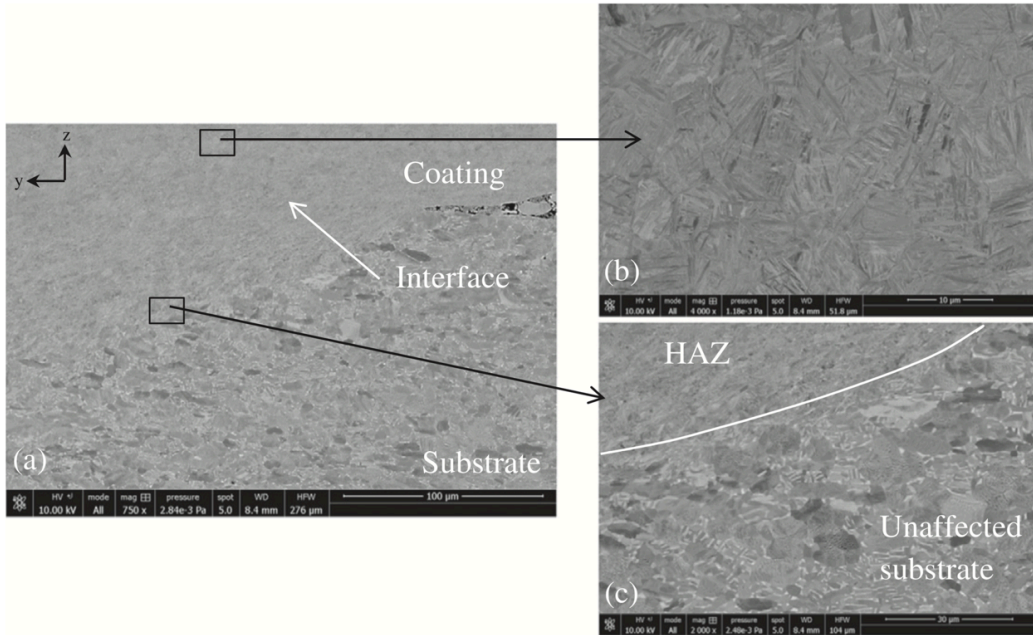


Figure 2.3: Microstructure evolution at Ti-6Al-4V coating. (a) overview, (b) coating and (c) HAZ and unaffected substrate [Fitseva et al., 2016].

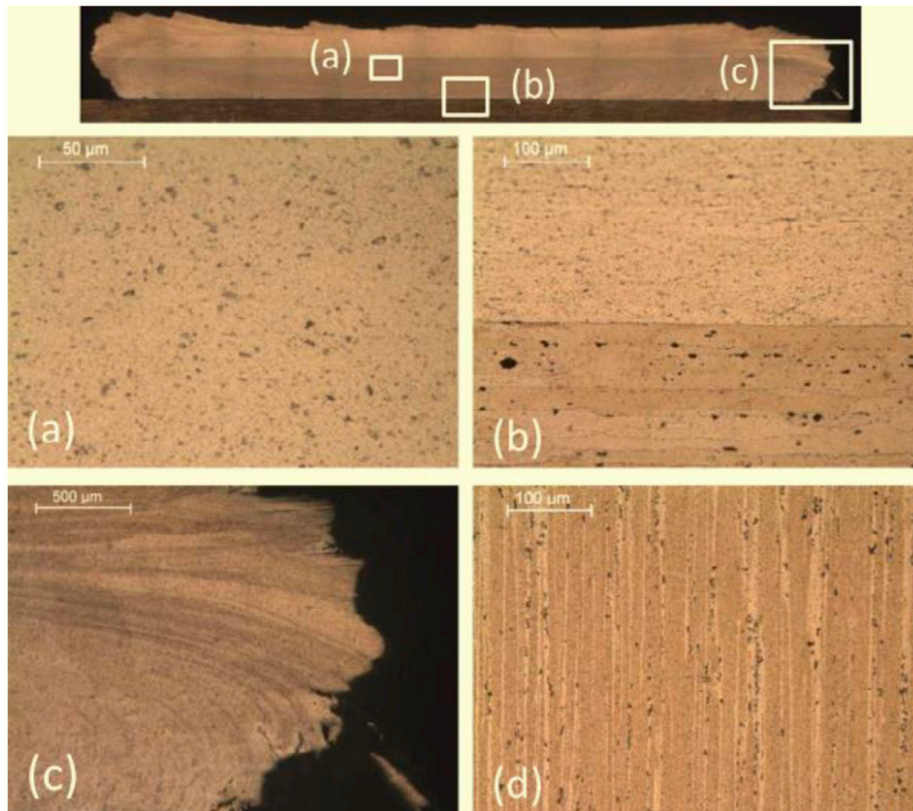


Figure 2.4: Coating cross section macrograph; (a) coating; (b) bonding interface; (c) unbonded edge; (d) as-received consumable rod [Gandra et al., 2013].

**Process control parameters** The FS deposition process is controlled by the following parameters:

- Axial force  $F_z$ . It can be seen as a forging force during the plastification step. An increase in axial force can produce wider and thinner coatings and improves the bonding strength for AA6082 according to [Gandra et al., 2013].
- Rod consumption rate  $V_{CR}$ . This parameter is directly related to the axial force and during FS deposition one of the two is controlled, and the other measured. According to [Fitseva et al., 2015], Grade 1 Ti depositions are more stable in consumption rate controlled mode. AA6082 depositions are possible in constant axial force mode.
- Rotational velocity  $\Omega$ . Controls the heat input into the coating. For Ti-6Al-4V according to [Fitseva et al., 2015] an increase in rotational velocity leads to wider and thicker coatings. The opposite effect was observed by [Gandra et al., 2013] for AA6082, where both coating thickness and width decreased with rotational velocity increase.
- Translational velocity  $V_{tr}$ . Affects the coating cooling rate during the deposition. Increase in  $V_{tr}$  has been reported to decrease coating thickness for AA6082 by [Gandra et al., 2013]. For Ti-6Al-4V lower translational velocities lead to higher heat input, deeper heat affected zone and thicker coatings according to [Fitseva, 2016].

Depositions are usually successful within a tight parameter window determined by the coating and substrate materials, and for each material parameter adjustments have different effects on the deposition process. For Grade 1 Ti and Ti-6Al-4V a PhD thesis by [Fitseva, 2016] presents a thorough investigation of the FS deposition parameters and their effect on the coating microstructure and geometry. For AA6082 on AA2024 a parameter study was published by [Gandra et al., 2013], and a comparative parameter study of AA6082 and AA5083 coatings was published by [Hanke and dos Santos, 2017]. The choice of deposition parameters for this study for all investigated cases (Ti-6Al-4V on Ti-6Al-4V, AA6082 on AA2024, AA5083 on AA2024) was based on [Fitseva, 2016] and [Hanke and dos Santos, 2017].

**Deposition efficiency** One of the metrics of the FS process is deposition efficiency. Deposition efficiency  $\eta$  is the ratio of the material deposition rate over stud consumption rate, i.e. it reveals which fraction of the processed stud material was deposited, and which was lost to the flash [Gandra et al., 2014]:

$$\eta = \frac{DR}{CR}. \quad (2.1)$$

In Eq. 2.1  $DR$  is the volumetric deposition rate defined as translational velocity multiplied by coating's cross-section area orthogonal to the deposition direction

$$DR = V_{Tr} \cdot A_c, \quad (2.2)$$

and  $CR$  is volumetric stud consumption rate defined as axial stud velocity multiplied by stud's cross-section area

$$CR = V_{Ax} \cdot A_s. \quad (2.3)$$

The cross-section area of a coating  $A_c$  is not easy to measure because of the coating's irregular shape. So with constant translational velocity and using an average value for the stud consumption rate, one can evaluate eqs. 2.1, 2.2, 2.3 as

$$\eta = \frac{V_{Tr} \cdot A_c}{V_{Ax} \cdot A_s} = \frac{\delta y \cdot A_c}{\delta z \cdot A_s} = \frac{\delta y \cdot A_c \cdot \rho \cdot z}{\delta z \cdot A_s \cdot \rho \cdot z} = \frac{\delta y \cdot A_c \cdot \rho}{A_s \cdot \rho \cdot z} \cdot \frac{z}{\delta z} = \frac{\delta m}{m} / \frac{\delta z}{z}. \quad (2.4)$$

Eq. 2.4 shows that for the conditions of this study the deposition efficiency  $\eta$  can be calculated as the relative mass loss of the stud divided by its relative length loss. The relative mass loss shows how much material was deposited on the substrate (the loss of material to the flash is not included in the stud mass loss, since the flash is attached to the stud after the deposition), and the relative length loss shows how much stud material was spent. Hence, their proportion is the deposition efficiency.

## 2.2 Residual stresses in welding processes

**Definitions** Residual stresses are forces that remain in a body that is stationary and at equilibrium with its surroundings [Withers and Bhadeshia, 2001]. Residual stresses can be categorized by the length scale over which they self-equilibrate. By convention there are three types: type I macrostresses that vary continuously over macroscopic distances, type II that vary over the grain scale, and type III that vary on the atomic scale.

For a cubic volume element with plane area  $A$  and forces  $F_i$  acting on it, the stress tensor  $\sigma_{ij}$  is defined to be force per area acting on face  $i$  in direction  $j$  [Hauk, 2010]:

$$\sigma_{ij} = \frac{F_i \cdot n_j}{A}, \text{ where } n_i \perp A, |n_i| = 1. \quad (2.5)$$

The strain tensor  $\varepsilon_{ij}$  is defined by derivatives of material displacements  $u_i$ , where  $u_i(x)$  is the displacement vector of point  $x$  [Hauk, 2010]:

$$\varepsilon_{ij} = \frac{1}{2}(\partial_j u_i + \partial_i u_j) = \frac{1}{2}(u_{i,j} + u_{j,i}). \quad (2.6)$$

It is possible to choose such coordinate system called *the principle axes* that  $\sigma$  becomes diagonal [Hauk, 2010].

**Hooke's Law** For isotropic systems principal stresses  $\sigma^D$  and strains  $\varepsilon^D$  are connected by Hooke's Law [Allen et al., 1985]:

$$\begin{pmatrix} \sigma_{11}^D \\ \sigma_{22}^D \\ \sigma_{33}^D \end{pmatrix} = \frac{E}{1+\nu} \begin{pmatrix} \varepsilon_{11}^D \\ \varepsilon_{22}^D \\ \varepsilon_{33}^D \end{pmatrix} + \frac{\nu E (\varepsilon_{11}^D + \varepsilon_{22}^D + \varepsilon_{33}^D)}{(1-2\nu)(1+\nu)} \begin{pmatrix} 1 \\ 1 \\ 1 \end{pmatrix} \quad (2.7)$$

In Eq. 2.7 elasticity modulus  $E$  and Poisson number  $\nu$  are material specific constants and can be found in literature for most commonly used engineering materials.

In case of biaxial or plane stress state where  $\sigma_{33} = 0$  Hooke's Law takes a simpler

form [Allen et al., 1985]:

$$\begin{pmatrix} \sigma_{11}^D \\ \sigma_{22}^D \end{pmatrix} = \frac{E}{1-\nu^2} \begin{pmatrix} \varepsilon_{11}^D \\ \varepsilon_{22}^D \end{pmatrix} + \frac{E\nu}{1-\nu^2} \begin{pmatrix} \varepsilon_{22}^D \\ \varepsilon_{11}^D \end{pmatrix} \quad (2.8)$$

$$\varepsilon_{33}^D = -\frac{\nu}{1-\nu}(\varepsilon_{11}^D + \varepsilon_{22}^D) \quad (2.9)$$

Eqs. 2.8, 2.9 can be used when one dimension of the system is much smaller than two other dimensions, and it can be assumed that no macrostresses develop over such short distance. For butt welds of sheet metal a typical assumption is that there are no stresses orthogonal to the sheet.

**RS in welding processes** There are at least four ways in which type I stresses can arise: through interaction of parts within an assembly, and through the generation of chemical, thermal, or plastically induced misfits between regions within one part [Withers and Bhadeshia, 2001].

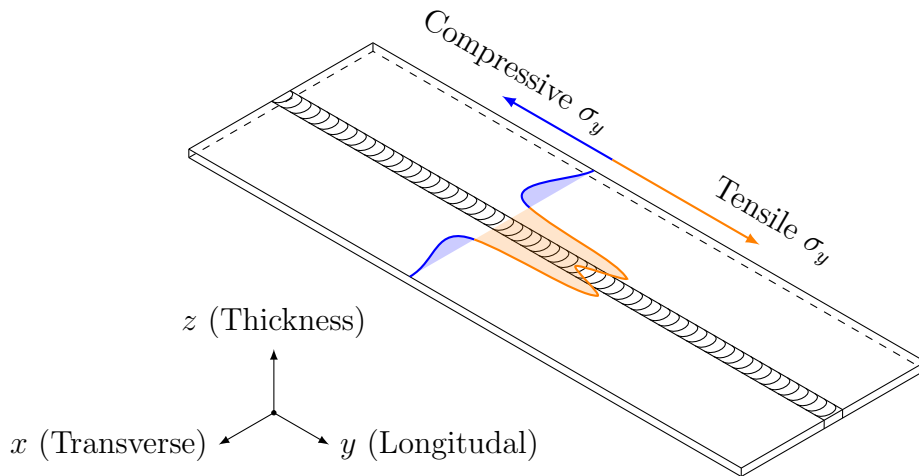


Figure 2.5: Typical longitudinal RS distributions for butt-welded joints.

In welding processes, large thermal stress gradients are caused by localised heating and subsequent cooling of the weld zone. A typical RS distribution for butt welded sheets according to the textbooks [Masubuchi, 2013] and [Radaj, 2012] looks like Fig. 2.5. The high tensile stress area around the weld seam is called the *active zone*. It is a direct consequence of the local heat application. The active zone may or may not have a drop in the middle due to the material plastic flow. This stress configuration with steep gradients on edges and a drop in the middle is called “M-shape” and is present in various welding processes. The compressive stress area around the active zone is

called the *compensative zone*. These compressive stresses are formed to balance the tensile stresses in the active zone.

According to [Masubuchi, 2013], since the RS exist without external forces, the resultant force produced by them must vanish:

$$\int dA \sigma = 0 \text{ on any plane section.} \quad (2.10)$$

A special case of the Eq. 2.10 applicable to the stress scans over the transverse direction  $x$  performed in this study:

$$\int dx \sigma_y(x) = 0. \quad (2.11)$$

**Measurement techniques** There are multiple methods to measure RS. The observed stresses depend on the used measurement method and chosen sampling volume [Withers and Bhadeshia, 2001]. For each sampling volume the measurements usually show the sum of all present stresses, so distinguishing between the types of RS requires careful consideration.

In this study the primary interest is in type I RS. There are several mechanical methods for measuring type I stresses, that work by gradually removing material from the part and observing the material movement. This includes hole drilling, incremental layer removal, contour method, and crack compliance method. While these methods allow for direct observation of the mechanical effects of the RS, they are destructive and provide limited information on the RS distribution for each investigated part.

For this study, non-destructive methods were chosen as the main probing tool, namely neutron and X-ray diffraction. In addition to measuring RS these methods can provide useful information on phase content, microstructure, temperature, chemical composition, and other parameters. Additionally fatigue crack propagation tests were performed to probe the mechanical properties directly. Specifics of method application to the current work are presented in Chapter 3.

# Chapter 3

## Experimental Techniques

### 3.1 Diffraction techniques

**Main principles** Diffraction occurs when radiation with wavelength  $\lambda$  comparable to atomic spacings is scattered by the atoms of a crystalline solid and undergoes constructive interference. This leads to Bragg's law, which describes the condition on the scattering angle  $\Theta$  for the constructive interference to be at its strongest:

$$n\lambda = 2d \sin \Theta, \quad n = 1, 2, \dots \quad (3.1)$$

Eq. 3.1 connects the scattering angle of an observed diffraction peak  $\Theta$  and incident wavelength  $\lambda$  to the crystal's interplanar distance  $d$ . In a typical diffraction experiment one controls the setup parameter  $\lambda$ , measures the observable  $\Theta$  and from them calculates the crystal structure parameter  $d$ .

Using Bragg's law the strain  $\varepsilon$  in the direction normal to a chosen lattice plane can be calculated as [Hauk, 2010]:

$$\varepsilon = \frac{\Delta d}{d_0} = -\Delta\Theta \cdot \cot(\Theta_0). \quad (3.2)$$

In Eq. 3.2  $\Delta\Theta$ ,  $\Delta d$  are changes in the scattering angle and lattice spacing respectively, from their corresponding values  $\Theta_0$ ,  $d_0$  for a stress-free sample. The angles  $\Theta$ ,  $\Theta_0$  are measured in radians. Eq. 3.2 allows to derive interplanar strains for any crystallographic direction in single crystals and polycrystalline samples.

The focus of this work is estimating macroscopic stresses in fine-grained polycrystalline samples. According to [Hutchings et al., 2005], this can be done by determining the strain for a lattice plane that is known to be least affected by the microstrain, and use bulk values of  $E$ ,  $\nu$  in Hooke's Law. In the materials used in this study lattice planes least affected by microstrain are: cubic Al (311) and  $\alpha$ -Ti (102) and (103) [Hutchings et al., 2005].

With the focus on measuring volumetric macroscopic stresses, the types of experiments chosen for the study were: X-ray diffraction in transmission geometry, X-ray diffraction with conical slits, and angle-dispersive neutron diffraction. The following paragraphs describe the specifics of each experiment type.

**X-ray diffraction in transmission geometry** The setup for in-transmission X-ray diffraction measurements is shown on Fig. 3.1. The incoming beam penetrates the sample at the right side and exits it at the left side delivering diffraction cones. In this setup the gauge volume is defined by the forming slit and sample positionig, and the obtained data represents information integrated along the sample  $z$  axis with no depth-resolved information.

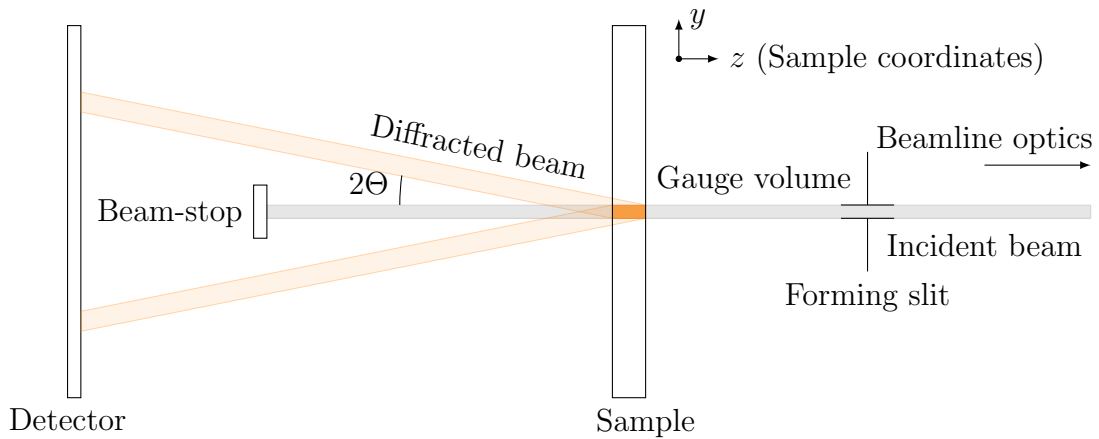


Figure 3.1: Setup for in-transmission diffraction measurements using synchrotron radiation.

The configuration was realised at the HZG beamline P07B located at PETRA III at DESY. The photon energy at this beamline is fixed at 87.5 keV. At this energy the  $2\theta$  angles for relevant Bragg reflexes are less than  $10^\circ$ , so with the sample  $xy$  plane orthogonal to the incident beam, diffraction rings represent  $\varepsilon_x$ ,  $\varepsilon_y$  closely. The

beamline is equipped with a Perkin-Elmer detector with an active area of  $400 \text{ mm} \times 400 \text{ mm}$  and resolution  $2048 \text{ pix} \times 2048 \text{ pix}$ . The detector position was chosen to have the relevant rings fully in view, as shown on Fig. 3.2.

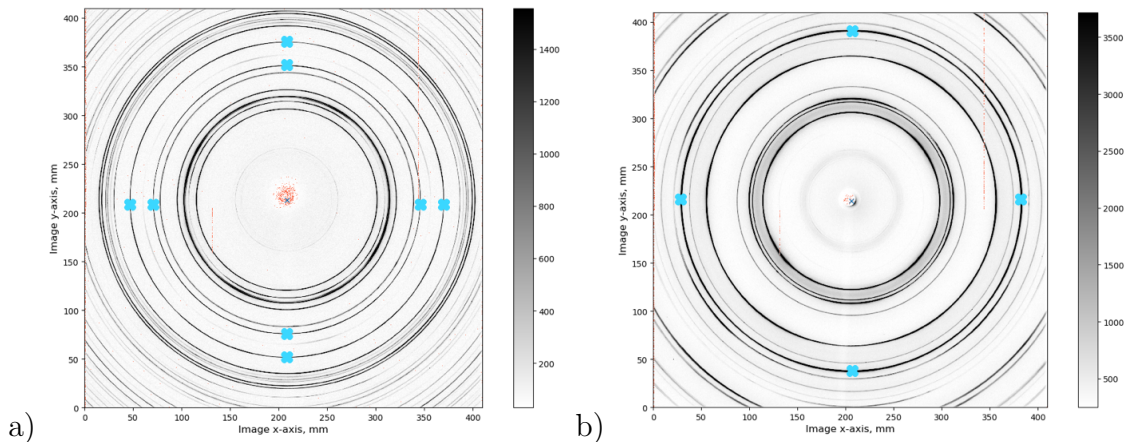


Figure 3.2: Typical detector images from the synchrotron diffraction experiments at P07B beamline at DESY. a) Ti-6Al-4V plate with Cu powder reference, b) AA2024 plate with Cu powder reference. Relevant reflexes a)  $\alpha$ -Ti (102), (103) and b) Al (311) are marked with blue crosses.

Since this setup requires sample-detector distance calibration, Cu powder paste was applied to each sample and used as a calibrant for every detector image. Since the investigated FS coatings have thickness  $\sim 2.2 \text{ mm}$ , the sample-detector distance for the diffraction images of the coated area was corrected by  $1.1 \text{ mm}$ .

**X-ray diffraction with conical slits** The setup for the conical slit X-ray diffraction measurements is shown on Fig. 3.3. Similarly to the transmission geometry setup on Fig. 3.1, the beam penetrates the sample at the right side and exits on the left, delivering diffraction cones. A conical slit system is used to define the gauge volume and allow to collect series of diffraction patterns from different depths along the sample  $z$  axis [Staron et al., 2014].

The configuration was realised at the HZG beamline P07B located at PETRA III at DESY. As mentioned previously, the photon energy at this beamline is fixed at  $87.5 \text{ keV}$ . This means that a special conical slit has to be used for every material, with a specific conical aperture suited for this material's relevant Bragg reflex. In this case a conical slit for cubic Al (311) reflex was used.

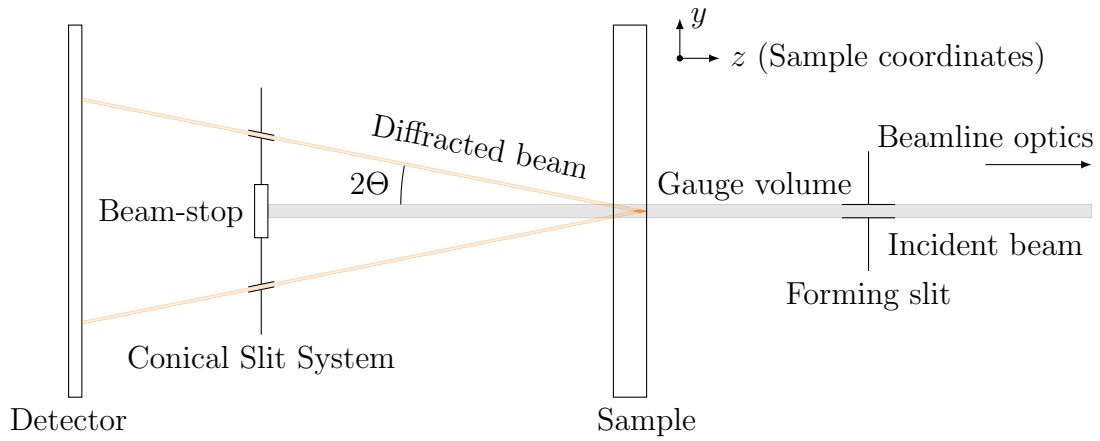


Figure 3.3: Setup for stress-diffractometry using synchrotron radiation and conical slits.

A typical detector image from this experiment can be seen on Fig. 3.4. For this type of experiment the noise to signal ratio is an issue due to a small gauge volume. More than one ring is visible due to a different Bragg reflex coming from another gauge volume within the sample.

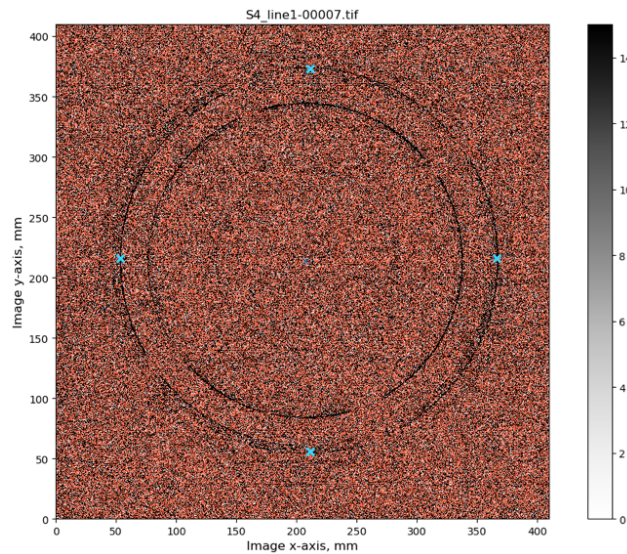


Figure 3.4: Typical detector images from the synchrotron diffraction with conical slit experiments at P07B beamline at DESY. Relevant reflex Al (311) is marked with the blue crosses.

**Angle-dispersive neutron diffraction** In order to measure the full strain tensor in the samples used in this study, penetration depth of neutrons and gauge volume definition of neutron setups was required.

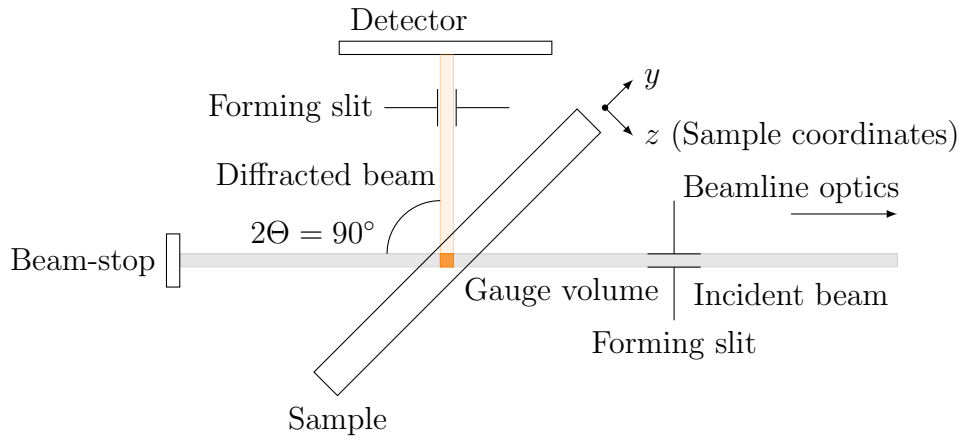


Figure 3.5: Setup for stress-diffractometry using constant wavelength neutron radiation.

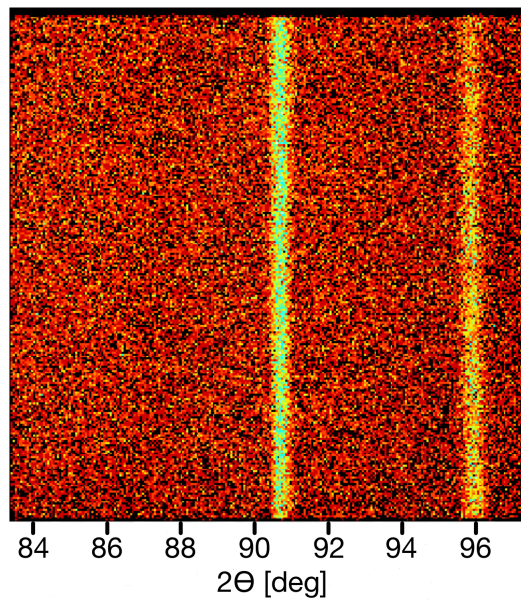


Figure 3.6: Typical detector images from the neutron diffraction at STRESS-SPEC instrument at FRM II reactor. The relevant reflex Al (311) is at the center.

Neutron stress-diffractometry was performed at HZG instrument STRESS-SPEC at the FRM II research reactor. Fig. 3.5 shows the experimental setup configuration. At this setup, the incident beam wavelength can be adjusted, so that the relevant Bragg reflex of the sample material is at  $2\Theta \simeq 90^\circ$ . This allows for definition of a cubic gauge volume by two sets of slits, which in turn lets the user obtain  $\varepsilon_x$ ,  $\varepsilon_y$ , and  $\varepsilon_z$  by rotating the sample and selecting the same gauge volume each time.

The STRESS-SPEC instrument is equipped with a  $256 \text{ pix} \times 256 \text{ pix}$  position-sensitive detector. A typical detector image from the experiment can be seen on Fig. 3.6. The

detector collects a section of the diffraction ring, so one exposure provides information on one strain tensor component:  $\varepsilon_x$ ,  $\varepsilon_y$ , or  $\varepsilon_z$ .

The downside of neutron diffraction is slow data acquisition speed, with one exposure time being 10–20 min depending on how deep in the sample the gauge volume is. The same gauge volume can be exposed at synchrotron beamline P07B in  $\sim 1$  s. Neutron diffraction can provide more information about the strain tensor, but at much slower speed compared to the X-ray diffraction.

**Diffraction data analysis** The data analysis pipeline can be separated into the following stages:

1. Detector image calibration / integration;
2. Peak (profile) fitting;
3. Calculating stress and estimating  $d_0$  from force balance (Eq. 2.11);
4. Calculating stress with the estimated  $d_0$  value.

Steps 1 and 2 require specialised software. GSAS II [Toby and Von Dreele, 2013] and STeCa [Randau et al., 2011] were used for performing steps 1-2 on the synchrotron and neutron diffraction data respectively. Steps 3-4 can be performed in any software capable of working with data structures, so Python 3.6 and SciPy library were used [McKinney, 2010].

## 3.2 FCP Testing

In order to compare the residual stress estimations done by diffraction with the mechanical properties of the FS coated samples, Fatigue Crack Propagation (FCP) tests were performed on C(T) samples cut from the coated sheets. Fig. 3.7 shows the sample geometry. The idea behind the FCP testing is to grow a crack from an initial notch by applying a load to the pin holes. By comparing the crack growth rate between the welded and the base material samples one can estimate the stresses introduced to the base material by the welding process.

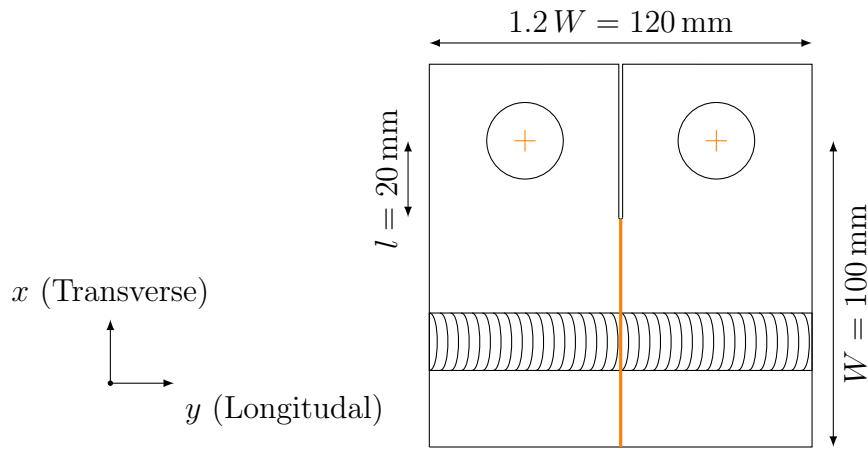


Figure 3.7: Geometry of C(T) samples used in the study. The orange line marks the crack propagation direction. Crosses mark the points of load application.

As a part of the investigation presented in Chapter 4, FCP tests were performed on a set of three Ti-6Al-4V base material samples, on a set of three samples coated with translational stud speed 24 mm/s and a set of three samples coated with 8 mm/s. C(T) samples were cut to width  $W = 100$  mm using electrical discharge machining (EDM). The C(T) sample thickness was  $B = 2$  mm. The tests were performed at a constant force amplitude in agreement with [ASTM, 2008]. No pre-cracking procedure was followed. The force amplitude was  $F = 1.28$  kN for two of the base material samples, and  $F = 2.44$  kN for the third base material sample and for the coated samples. The force ratio was  $R = 0.1$ , the frequency  $f = 10$  Hz. The initial notch size was  $l = 20$  mm, the crack length was controlled with an optical microscope, and the crack propagation direction was orthogonal to the coating deposition direction.

### 3.3 Temperature measurements during Friction Surfacing coating deposition

In order to determine the heat input into the substrate during the FS coating deposition, temperature measurements were performed. The thermocouples were mounted as shown on Fig. 3.8 between the substrate bottom and the backing plate, so that the thermal state of the substrate was not affected by the measurements. For each temperature measurement three type K thermocouples were used, and the mean value taken as a result. The data was collected from thermocouples at a sampling rate of 10 Hz.

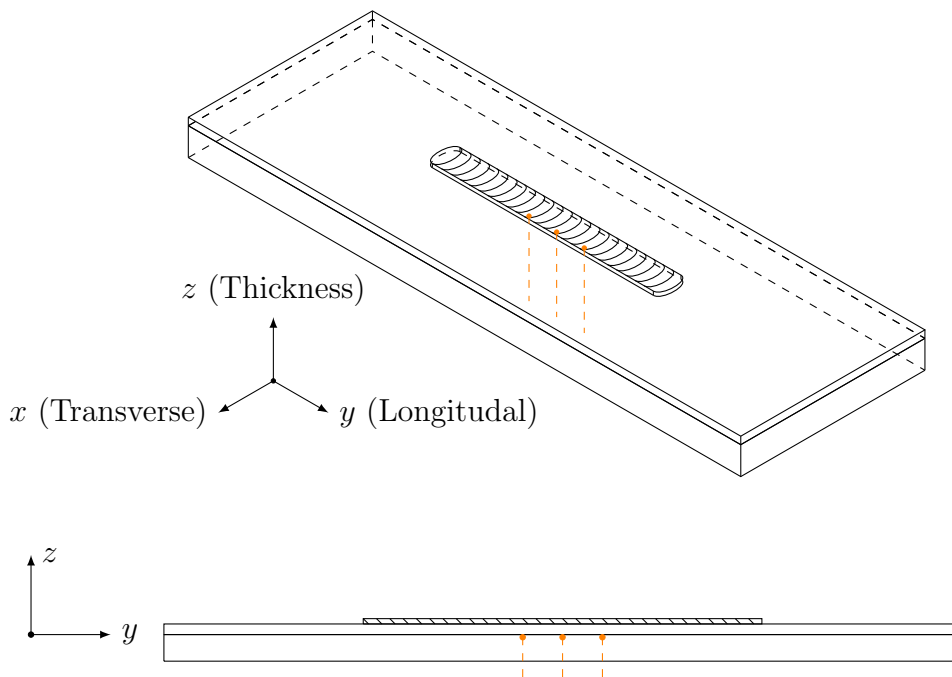


Figure 3.8: TC mounting scheme. TCs are connected to the bottom of the substrate, wires fed through the holes in the backing plate. The central TC is below the center of the coating, other two are  $\pm 20$  mm apart in  $y$  direction.

# Chapter 4

## Residual Stresses and Fatigue Crack Growth in Friction Surfacing Coated Ti-6Al-4V Sheets

### 4.1 Introduction

**Research topic** Ti-6Al-4V is the most commonly established modern Ti-based alloy. It has found a wide range of applications in industry, being lightweight and showing good temperature and corrosion resistance properties. However, there is still a demand to increase the resistance to wear and fatigue, aiming at higher loading capacity or longer service life of components.

In the following, the correlation between translational stud speed during FS and the RS state of the coated sheets are investigated. Both studs and sheets are from Ti-6Al-4V. Non-destructive synchrotron RS measurements are conducted to obtain residual stress distributions within the lateral sheet dimensions and FCP tests are carried out to observe the effect of RS on the cyclic material behaviour. This chapter is intended as a first step towards understanding RS formation in FS according to the process parameters.

Results presented in this chapter have been published as [Dovzhenko et al., 2018].

**Literature review** The relation between the RS state of a coated part and FS process parameters has to date not been published. The microstructural transformations in the FS coated Ti-6Al-4V sheets have been studied in-situ using high-energy X-ray radiation diffraction by [Hanke et al., 2017]. For FSW of Ti-6Al-4V, which is also a solid-state joining process, it is known that RS of varying magnitude may form in welded parts. In a study by [Muzvidziwa et al., 2016], RS in the weld surface were measured by X-ray diffraction in  $30\text{ mm} \times 30\text{ mm} \times 4\text{ mm}$  pieces that were cut from welds. RS in these were found to be in range of only 50 MPa or 5% of the yield strength. However, one could argue that RS in such small pieces can significantly relax during cutting; this would require further testing. Differences in crack growth behaviour within and outside the weld region in fatigue tests were attributed by the authors to the microstructural changes caused by FSW. A different study by [Edwards and Ramulu, 2015] on FSW of Ti-6Al-4V using a hole drilling method showed tensile RS in longitudinal direction on the sample surface in the weld region of up to 420 MPa ( $\sim 40\%$  yield stress) and compressive RS in transverse direction of  $-50$  to  $-200$  MPa.

A study by [Brewer et al., 2015] of FSW joined MA956 steel with neutron and synchrotron diffraction shows that the RS state is symmetric with regard to advancing and retreating sides with a slight drop towards the weld centre line (“M-shape”). They also found that the magnitude of the tensile RS in the weld region increases with increasing translational tool velocity. Similar observations were made by [Lombard et al., 2009] in a study of FSW joined AA5083-H321 alloy with synchrotron diffraction, and by [Peel et al., 2003] in a study of FSW joined AA5083 alloy also with synchrotron diffraction. [Pouget and Reynolds, 2008] also observed the M-shaped RS using cut compliance technique and found that fatigue crack propagation in friction stir welded AA2050 is strongly linked with the presence of RS. [Steuwer et al., 2012] in their study of FSW joined Ti-6Al-4V alloy using energy dispersive synchrotron radiation diffraction did not see the decrease of tensile RS in the weld centerline, but observed the similar correlation between RS and translational tool speed. The mentioned studies show that the welding speed has a strong influence on the heat input during FSW. A high heat input in a slow welding process leads to a larger softened material volume and lower cooling rates, which allows for a higher degree of material relaxation during cooling and therefore lower peak RS [Pouget and Reynolds, 2008].

## 4.2 Materials and experimental procedure

**Sample production** FS was carried out on an electrically driven, custom-built machine designed for small samples and low process forces. It is capable of delivering  $500 \text{ min}^{-1}$  to  $6000 \text{ min}^{-1}$  rotational speed, a torque of up to  $80 \text{ N} \cdot \text{m}$ , and a translational speed, carried out by the machine table, of up to  $20 \text{ mm/s}$ . In the current study, the rotational speed of the stud was kept constant and the translational speed was varied. The process was conducted in stud consumption rate mode, i.e. the stud was fed into the process zone at a constant axial speed. The applied process parameters are: rotational speed  $3000 \text{ min}^{-1}$ , stud consumption rate  $1.8 \text{ mm/s}$ , translational speeds  $8 \text{ mm/s}$ ,  $16 \text{ mm/s}$ ,  $24 \text{ mm/s}$ . Three samples were produced for each translational speed. The axial force, and the pressure acting in the stud-substrate interface is a resultant parameter. All set parameters as well as the spindle torque and the axial force on the stud were recorded by the welding equipment at a sampling rate of  $10 \text{ Hz}$ .

Studs of  $20 \text{ mm}$  diameter and  $120 \text{ mm}$  length were used to deposit coatings of approximately  $115 \text{ mm}$  length on sheets of  $2 \text{ mm}$  thickness and  $100 \text{ mm} \times 300 \text{ mm}$  width and length. The material for both coating and substrate was Ti-6Al-4V. A commercial purity copper sheet of  $2 \text{ mm}$  thickness was used as backing plate, between the coated substrate and the machine table, in order to enhance the heat flow.

Metallographic cross sections were prepared from coated sheets, perpendicular to the translational direction, by standard methods including polishing with diamond suspensions and etching using Kroll's reagent in order to reveal the heat-affected zone (HAZ) in the sheet.

Sample production and metallography were performed at the department of Solid State Joining Processes of Helmholtz-Zentrum Geesthacht by Stefanie Hanke (Helmholtz-Zentrum Geesthacht, Germany), Natalia Lopes do Vale (Universidade Federal de Pernambuco, Brazil) and Tobias Bucken (University of Duisburg-Essen, Germany).

**Diffraction measurements** X-ray diffraction measurements in transmission geometry were performed as described in Section 3.1. Three sheets coated with different

translational stud speeds were scanned as shown on Fig. 4.1, and one C(T)-100 sample as shown on Fig. 4.2. The scan line on the coated sheet is where the coating process has reached a stationary state, the C(T) sample scan line is the intended crack propagation direction. Each line was scanned with  $0.5 \text{ mm} \times 0.5 \text{ mm}$  beam cross-section and  $0.5 \text{ mm}$  step size. Area scans are compilations of  $\sim 4500$  diffraction patterns obtained with  $1.0 \text{ mm} \times 1.0 \text{ mm}$  beam and  $1.0 \text{ mm}$  step along both axes. Bulk values of the Ti-6Al-4V elastic constants were used in Hooke's law (Eq. 2.8): elasticity modulus  $E = 113.8 \text{ GPa}$ , Poisson number  $\nu = 0.34$ , yield strength  $\sigma_{yield} = 880 \text{ MPa}$  [Boyer and Gall, 1985].

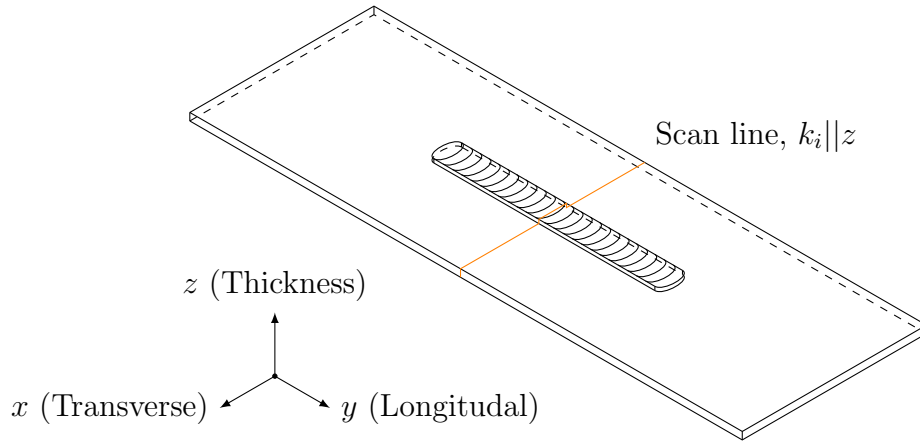


Figure 4.1: Coated sheet geometry and location of the synchrotron beam scan line.  $k_i$  (incident wave vector) is parallel to  $z$ . The sheet size is  $100 \text{ mm} \times 300 \text{ mm} \times 2 \text{ mm}$

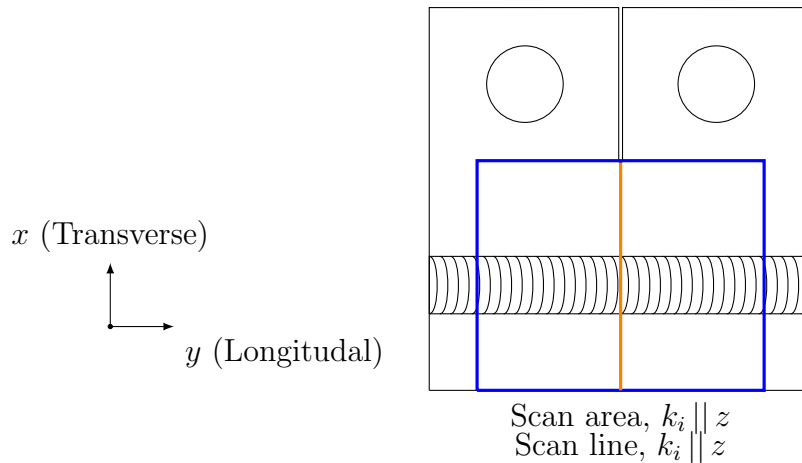


Figure 4.2:  $xy$  projection of C(T)-100 sample geometry with line ( $60 \text{ mm}$ ) and area ( $75 \text{ mm} \times 75 \text{ mm}$ ) scanned with the synchrotron beam.  $k_i$  (incident wave vector) is orthogonal to the image plane.

### 4.3 Results and discussion

**Translational speed and axial force** The change in translational speed was found to affect the axial force acting during the process. On Fig. 4.3, the axial force recorded by the equipment of three deposition runs at the three different translational speeds is plotted over the deposition length. The axial force changes over deposition time. Especially at 24 mm/s, it increases right after the start of the process with a peak value of 2.7 kN, and then stabilizes at 1.6 kN after 50 mm of deposition. At 16 mm/s translational speed, there is a peak of about 2.4 kN at the beginning, followed by a minimum below 1.0 kN before it also stabilizes at 1.6 kN after 50 mm deposition length. The slowest deposition of 8 mm/s speed displays a different behaviour. While it also requires time to stabilize the axial force, the stable force of 2.6 kN reached after 60 mm deposition length is higher than for the other two parameters. The appearance of the coatings does not reflect the variations in axial force. The produced coating is of homogeneous width and thickness throughout the deposition length (as on Fig. 2.2).

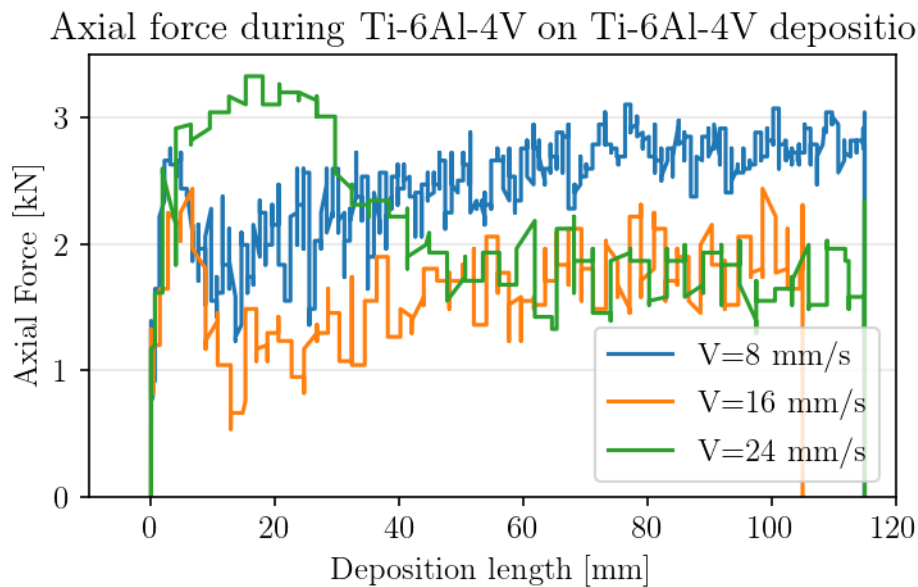


Figure 4.3: Dependence of axial force on weld length during deposition for different translational speeds.

Force fluctuations after the start of the process can be related to some time required to reach a steady state of temperature and material flow from the plasticized stud tip to the substrate. No pre-heating phase was included in the process procedure

since Ti-6Al-4V plasticizes immediately. Still, the heat generated from friction and plastic deformation is very localized in and under the deforming stud tip, as stated by [Liu et al., 2008] in their study of the theoretical basis for describing the FS process. As the process continues, heat conduction will lead to a rise in temperature of a larger volume of the stud tip, reducing the material strength and the shear forces required to reach plastification. The time it takes to finish a deposition layer depends on the translational speed, which also affects the force fluctuations before steady state is reached. Further, material is removed from the stud and deposited onto the substrate by shearing it off the plasticized stud tip. A higher translational speed will result in a faster removal of the material, allowing a lower dwell time in the plasticized regime. This means that the ratio of numbers of rotation vs. translational distance travelled decreases, as the translational speed increases. Nevertheless, after a sufficient process time or deposition length all three translational speeds result to an oscillating, but stable axial force. While for 24 mm/s and 16 mm/s, the force value is the same, observed for three deposition runs at each parameter set, the value for the lowest speed of 8 mm/s is significantly higher. This can be correlated with the coating thickness, i.e. the amount of material plasticized and deposited, as shown in the following sections.

**RS distributions in sheets** The shape of the RS curve observed in FS coated Ti-6Al-4V (Figs. 4.4, 4.5) corresponds with the shape usually observed in other welding processes (see Fig. 2.5). There is an active zone with high tensile stresses, coming from plastic strains that occurred during heating, deformation, and cooling, and the rest of the material is a compensative zone whose compressive stresses are decreasing with distance from the active zone in such a way that they compensate tensile stresses in the active zone. At 8, 16 and 24 mm/s translational velocities the peak tensile RS values are respectively 31%, 44%, 40% tensile yield strength and peak compressive RS values are 24%, 17%, 20% compressive yield strength. These results show difference from FSW on Ti-6Al-4V presented by [Edwards and Ramulu, 2015]. There the transverse RS are compressive at the centerline and in surrounding base material, as opposed to tensile in FS, but longitudinal RS show similar values and behaviour in both processes.

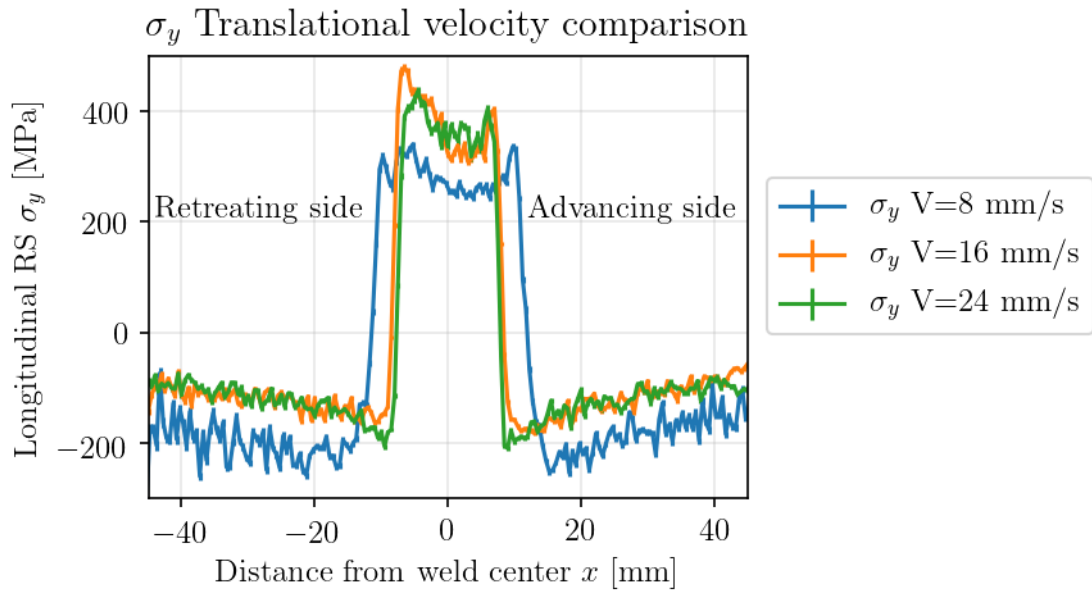


Figure 4.4: Longitudinal  $\sigma_y$  RS distribution along the scan line for Ti-6Al-4V coatings on the similar substrate.

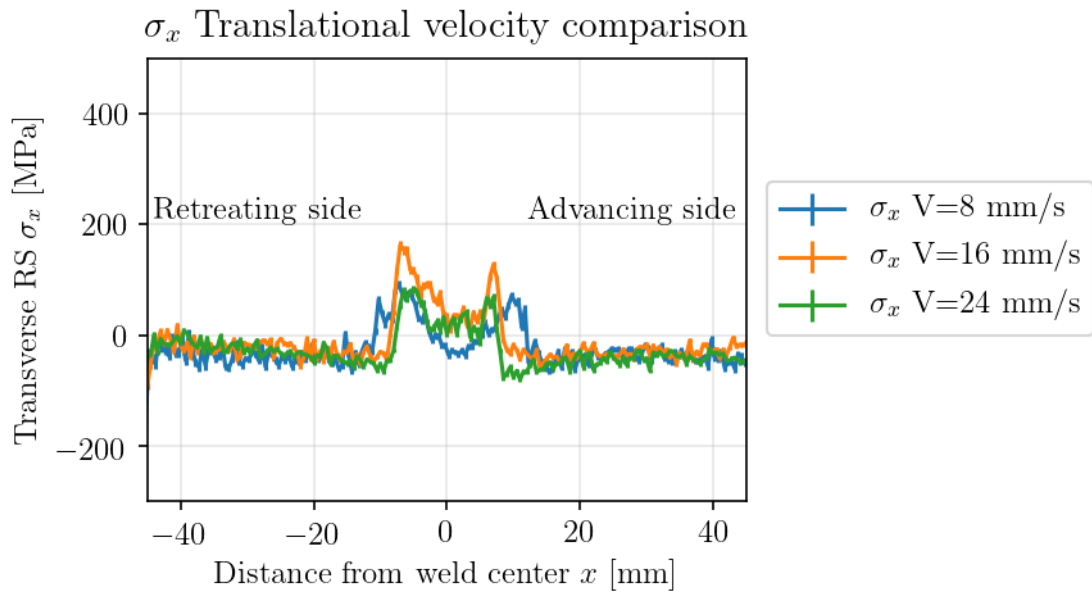


Figure 4.5: Transverse  $\sigma_x$  RS distribution along the scan line for Ti-6Al-4V coatings on the similar substrate.

Due to the asymmetric nature of FS process, there is a small difference in RS between advancing and retreating sides, and the fact that higher stresses are on the retreating side is opposed to FSW, where higher stresses are occasionally observed on the advancing side, as reported by [Sun et al., 2017]. A possible explanation is a significant

difference between the processes of FSW and FS. In FSW, the largest part of the material flows from the advancing side around the tool to the retreating, and then back to the advancing side, where the joint is consolidated. This behaviour was reported by [Hoyos et al., 2016] in their phenomenological based semiphysical modelling study on the process, and also by [Tongne et al., 2017] in finite element modelling study supported by optical and electron microscopy. In FS, torsional material flow in the process zone occurs, but the material volume being deposited was reported by [Rafi et al., 2011] to flow mainly from the advancing only to the retreating side, where it is stopped by the material previously deposited as coating layer.

In FS with change of translational stud speed, higher RS tend to correlate with a narrower active zone (Figs. 4.4, 4.5). A closer look on Fig. 4.6 shows that the broader tensile RS region of the low translational speed (8 mm/s) correlates with the larger coating width deposited at this parameter. At the same time, the coating has a significantly higher thickness and the heat affected zone (HAZ, brighter in the micrographs) includes the complete sheet thickness. The reason for this is the dwell time of the heat source (the rotating stud) being longer at lower translational speeds, and the overall heat input being higher. For the intermediate translational speed (16 mm/s), the RS distribution is comparable to the one at 24 mm/s, although here also a higher heat input must be assumed.

The coating thickness does not show a simple correlation with the translational speed. It ranges from 0.6 to 0.8 mm for 24 and 16 mm/s translational speed, while for 8 mm/s it is around 2.3 mm. The large material volume deposited at high temperature at 8 mm/s is possibly the reason why the active zone on the RS plots (Fig. 4.4, 4.5) and HAZ on the micrograph (Fig. 4.6 a)) is much wider compared to 16 and 24 mm/s translational velocity and reaches the bottom of the substrate. The peak RS values for 8 mm/s translational velocity are lower due to the material under the coating being more uniformly heated and plastically deformed. Also due to the larger cross-section the cooling rate was probably lower compared to 16 and 24 mm/s deposition velocity. For 16 and 24 mm/s translational velocity, the HAZ does not reach the bottom of the substrate, leading to harsher cooling boundary conditions and hence higher RS.

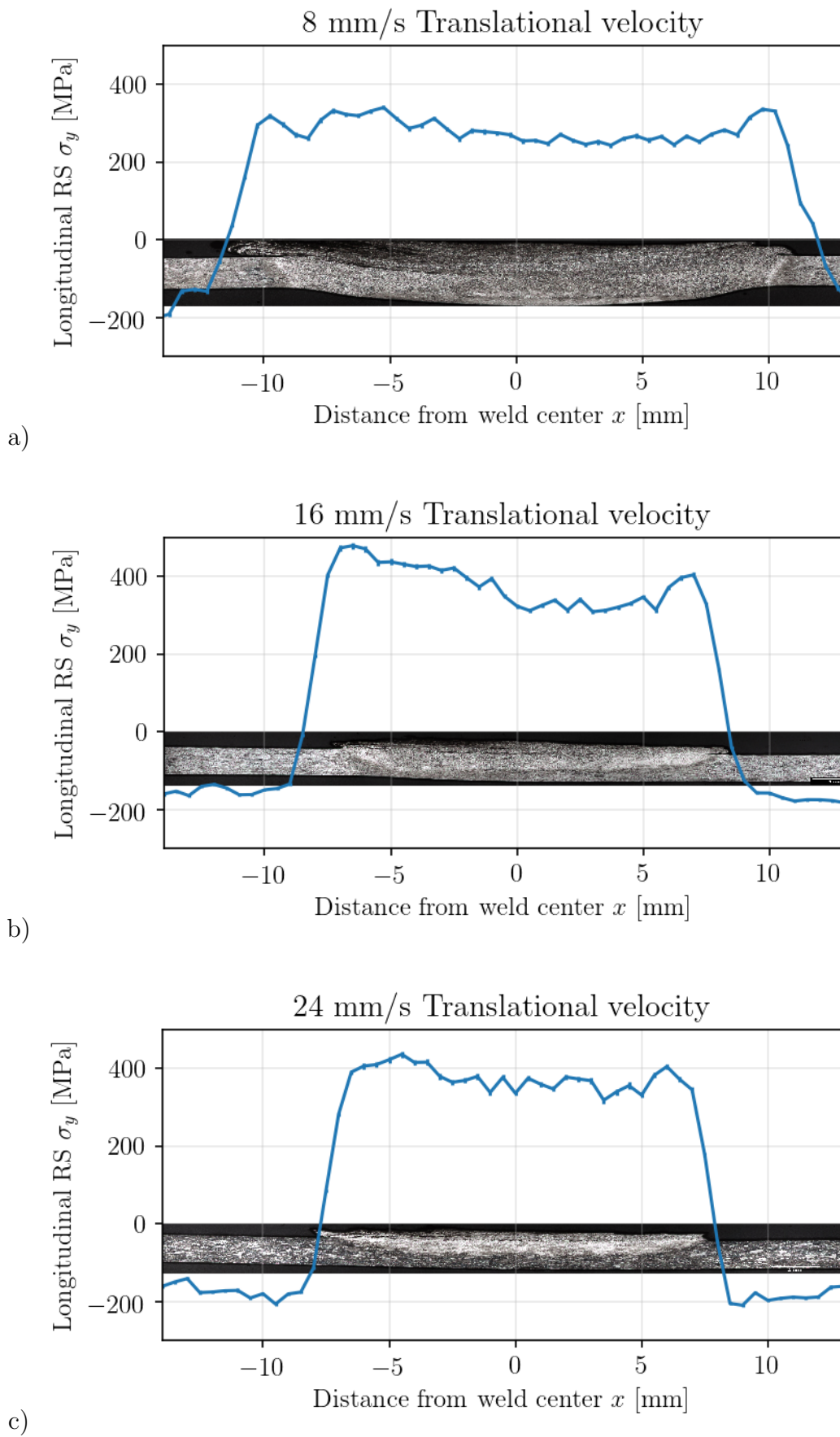


Figure 4.6: Longitudinal RS  $\sigma_y$  distribution along x axis in as-welded sheets and corresponding metallographic cross section for a) 8 mm/s, b) 16 mm/s, c) 24 mm/s translational stud speed.

**Fatigue properties** The constant force amplitude tests performed according to [ASTM, 2008] standard as described in Section 3.1. The base material has shown no anomalies for force amplitudes of  $F = 1.28$  kN and  $F = 2.44$  kN. The crack growth rate vs stress intensity factor range plots can be seen on Fig. 4.7. The data on a log-log scale was approximated with linear functions (Paris' Law) as was suggested by [Paris and Erdogan, 1963]:

$$\frac{da}{dN} = C \cdot (\Delta K)^m. \quad (4.1)$$

For the coated samples, force amplitude  $F = 1.28$  kN has yielded no crack initiation

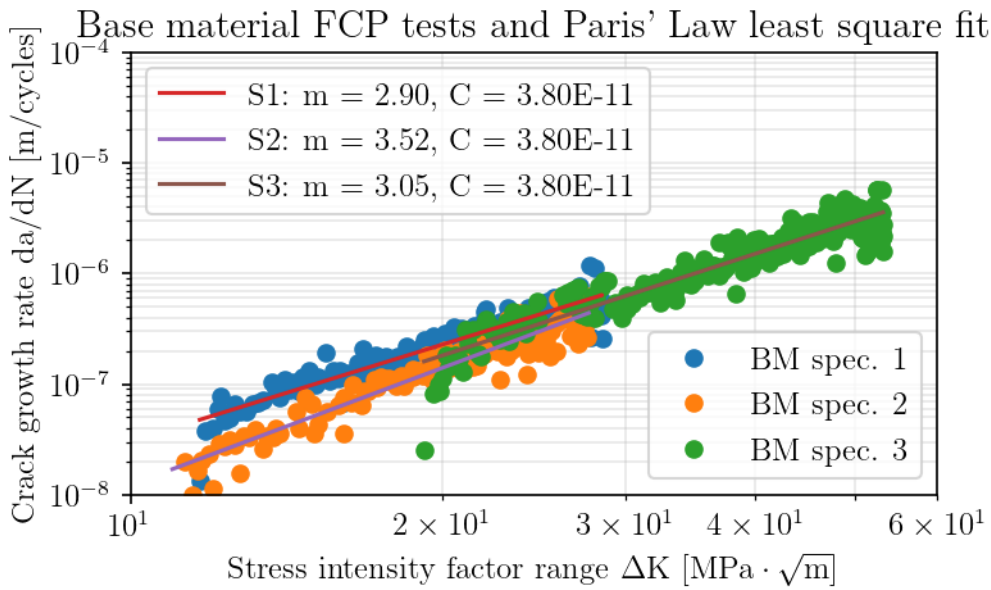


Figure 4.7: Crack growth vs stress intensity factor range for constant-force-amplitude tests on the substrate base material. Specimen 1 and 2 were tested with  $F = 1.28$  kN and specimen 3 with  $F = 2.44$  kN.

at the notch tip after  $5 \cdot 10^4$  cycles on samples coated both with 24 mm/s and 8 mm/s translational stud velocity. Under same conditions the two tested base material samples already had cracks of 3.9 mm and 4.2 mm length from the notch tip.

Force amplitude  $F = 2.44$  kN applied to the coated samples has yielded cracks starting at the notch tip diverged at an angle between  $30^\circ$  and  $45^\circ$ . Comparison of crack initiation time with fatigue behaviour of the base material sample is shown on Fig. 4.8. The improvement of lifetime before crack initiation is visible, and correlates with RS state of the coated samples: compressive  $\sigma_x$  orthogonal to the crack propagation

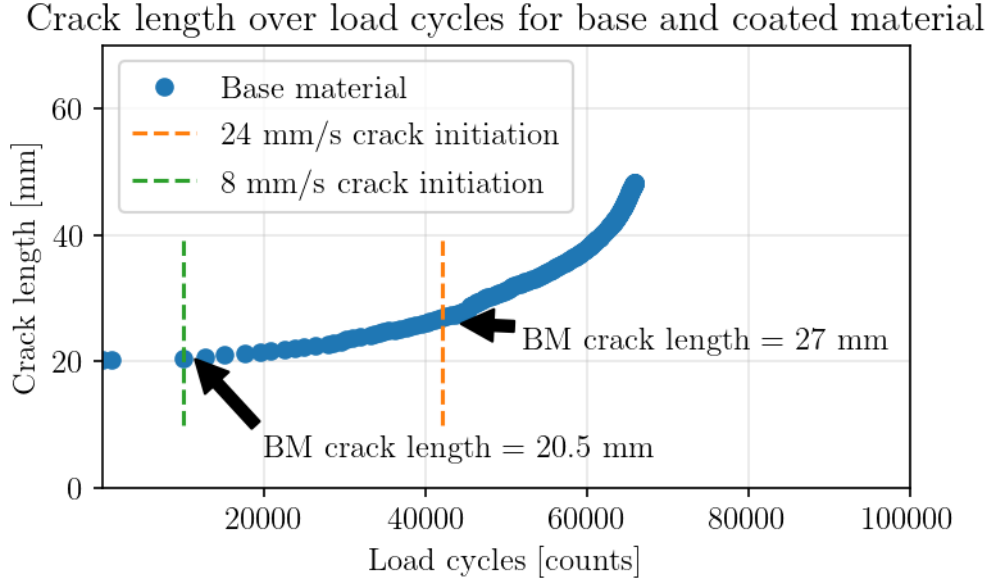


Figure 4.8: Crack length as a function of load cycles using  $F = 2.44$  kN amplitude for a Ti-6Al-4V base material sheet and number of cycles where the crack initiated at the notch tip for samples coated with two translational speeds. The notch length before loading was 20 mm in all cases.

direction  $y$  would delay crack initiation, and samples coated with 8 mm/s translational speed and having lower RS show a smaller improvement than the ones coated with 24 mm/s and having higher RS. In coated samples after 1 to 3 mm of a singular diverted crack propagation a second in most cases symmetric crack appeared (Fig. 4.9), and then both cracks propagated simultaneously. After 2.8 – 3.2 Mcycles no crack was able to reach the coating, in some cases by the end of the test cracks propagated parallel to it.

It is impossible to say if the RS are the only reason for crack initiation delay and crack diversion: other parameters, like sample bending or non-standard cross-section due to added material could also have played a role. This case requires further investigations in order to quantify the fatigue life more accurately. One of the possible follow-ups could be repeating the fatigue tests on annealed stress-free coated samples.

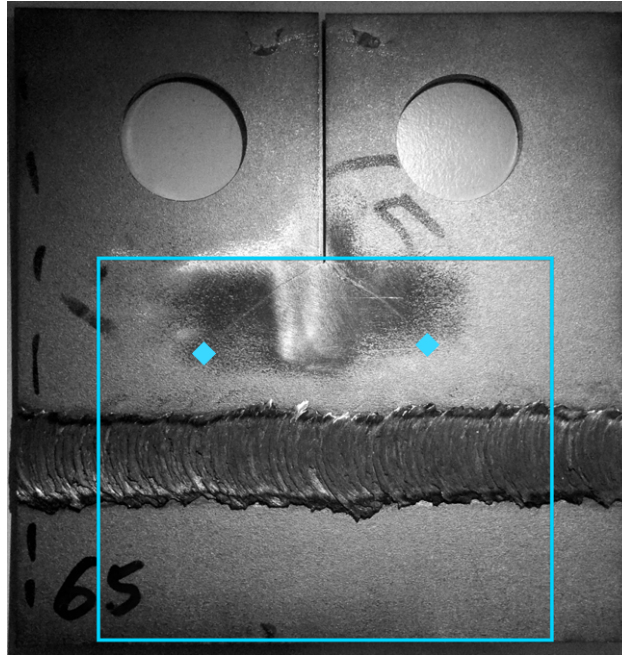


Figure 4.9: C(T) sample from a sheet coated with 24 mm/s after 4 Mcycles of FCP testing. Two symmetric cracks are visible (tips marked with blue diamonds), the RS scan area is marked with a blue rectangle.

**RS Distributions in C(T)-100 samples** After cutting the coated sheets to C(T)-100 shape, tensile stresses in the active zone remain the same, while the compressive stresses in the compensative zone grow higher, as the amount of stresses to compensate does not change, but the zone itself shrinks (Fig. 4.10). Thus, one has to keep in mind that the influence on fatigue crack propagation will be different in the studied C(T) samples and larger coated sheets or manufactured parts.

The RS state of the coated sample (translational speed 24 mm/s) is uniform along the deposition direction with slight decreases towards sample edges, as it should be expected because of the post-deposition cutting to C(T) shape (Fig. 4.11). Uniformity of the RS distribution supports the statement that the deposition process reaches the equilibrium and is reproducible.

After 4 Mcycles of the constant force amplitude FCP testing, compressive stresses build up below the cracks (Fig. 4.12). The compressive stresses in the compensative zone have to equalize the tensile stresses in the active zone. As the compensative zone itself shrinks due to the crack growth, the stress values rise. Tensile RS peaks can be observed at the crack tips and at the crack flank detached from the part of

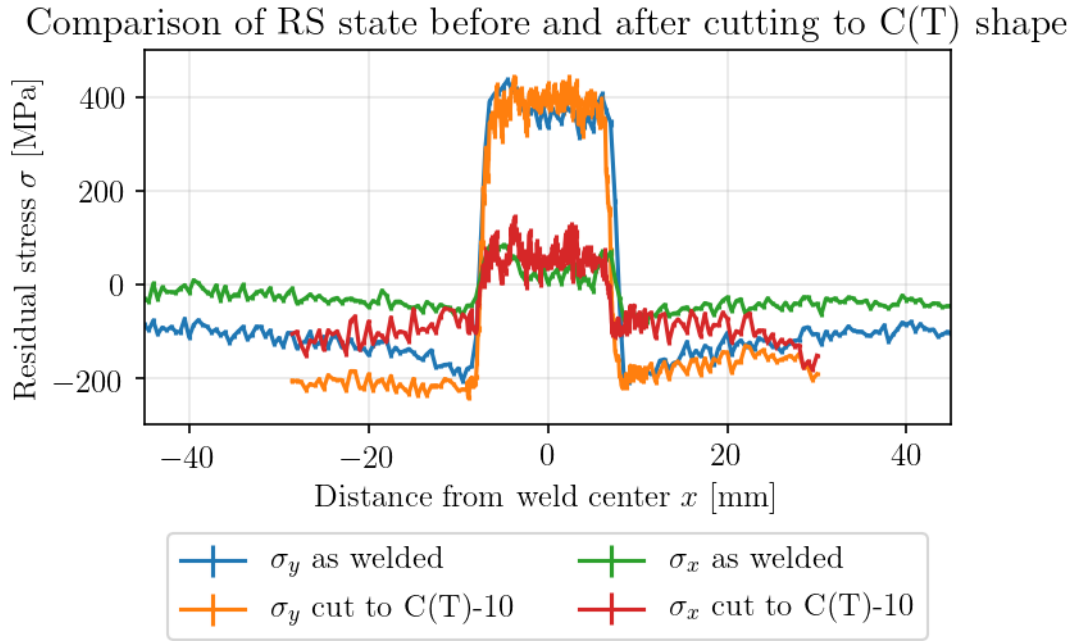


Figure 4.10: Comparison of RS distributions along the scan line in a coated with 24 mm/s tr. speed plate and a similar plate cut to C(T)-100 shape.

the sample containing the coating. A direct comparison of the before / after states is presented on Fig. 4.13. The  $\sigma_x$  peak values at the crack tips are significantly higher ( $\simeq 350$  MPa), than the  $\sigma_y$  peak values at the same position ( $\simeq 90$  MPa). This shows clearly the reason for the crack deviation towards the  $y$  direction and indicates that the further crack propagation will continue in this direction. This, together with the fact that two cracks form, is the reason for the slow crack propagation in the coated sheets. The C(T)-100 samples were chosen due to limitations in the sheet dimensions available for this study. It has been shown by [Shi et al., 1990] that particularly for this sample shape bending and rotation of the crack face may occur in the presence of RS, affecting significantly the test results. Larger M(T) samples have been found by [John et al., 2003] to display evaluable results for sheets containing FSW joints, which remains to be applied to FS coated sheets in the future.

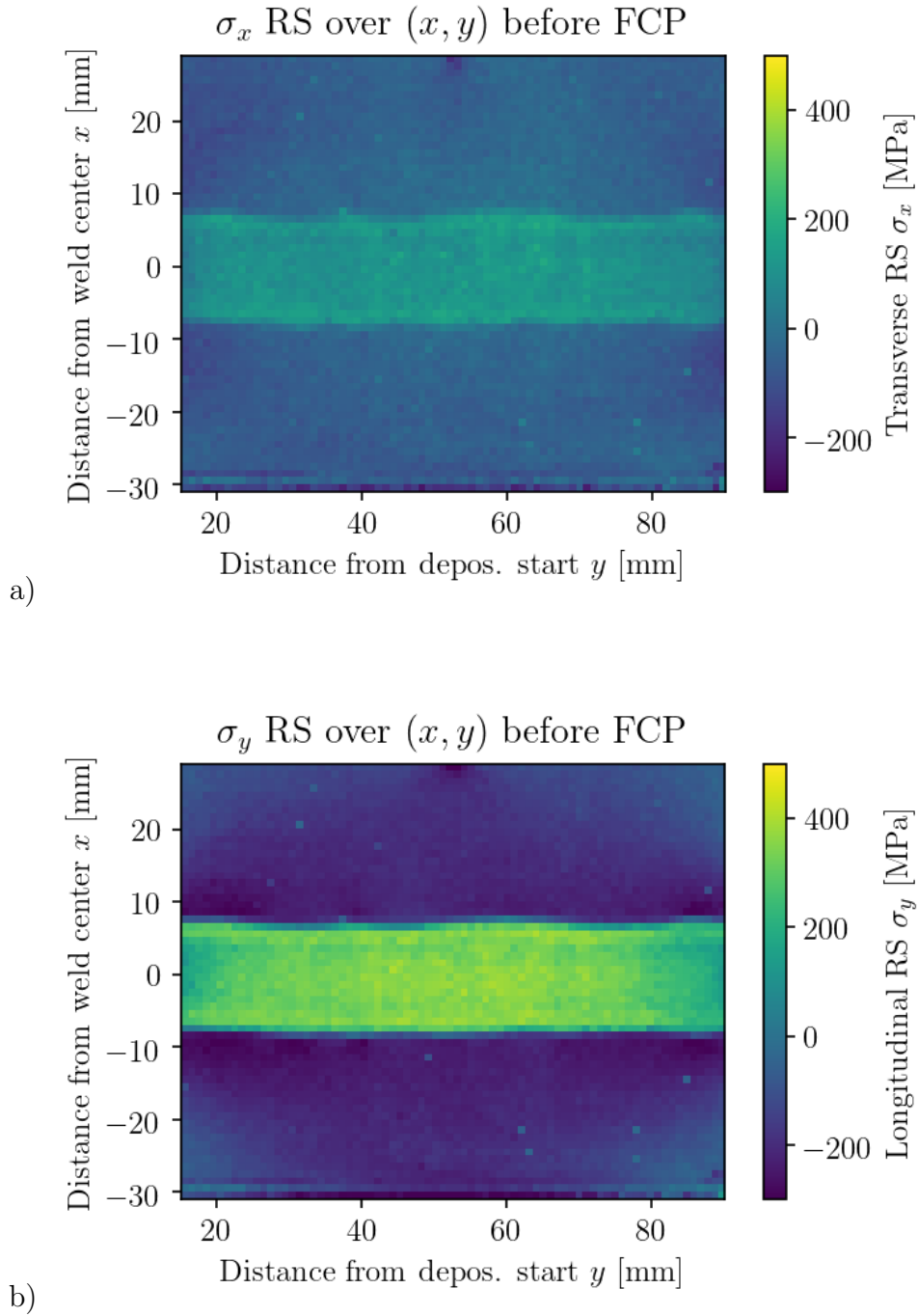


Figure 4.11: a) Transverse and b) Longitudinal RS in a C(T)-100 sample before testing within the scan area indicated in Fig. 4.2.

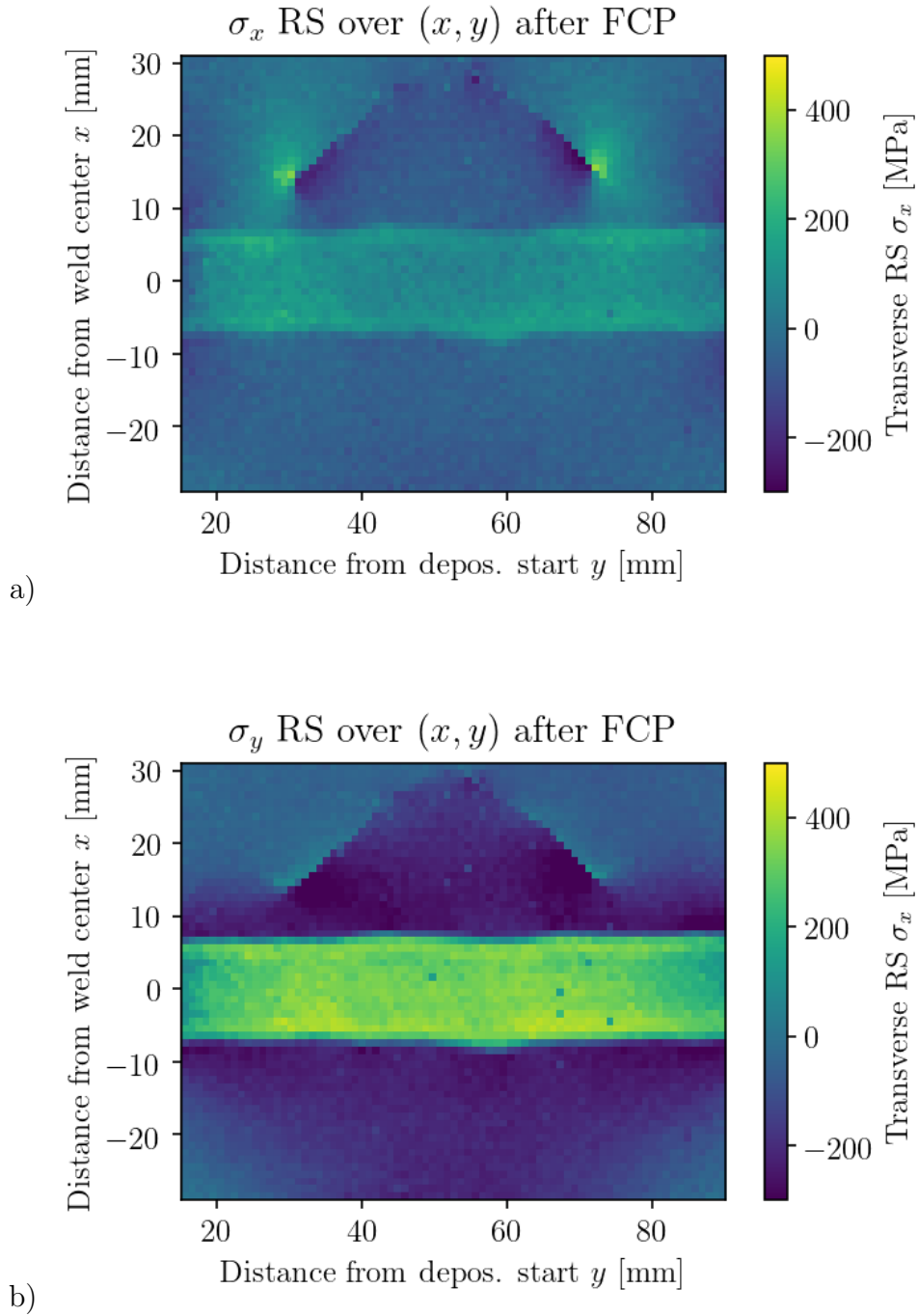
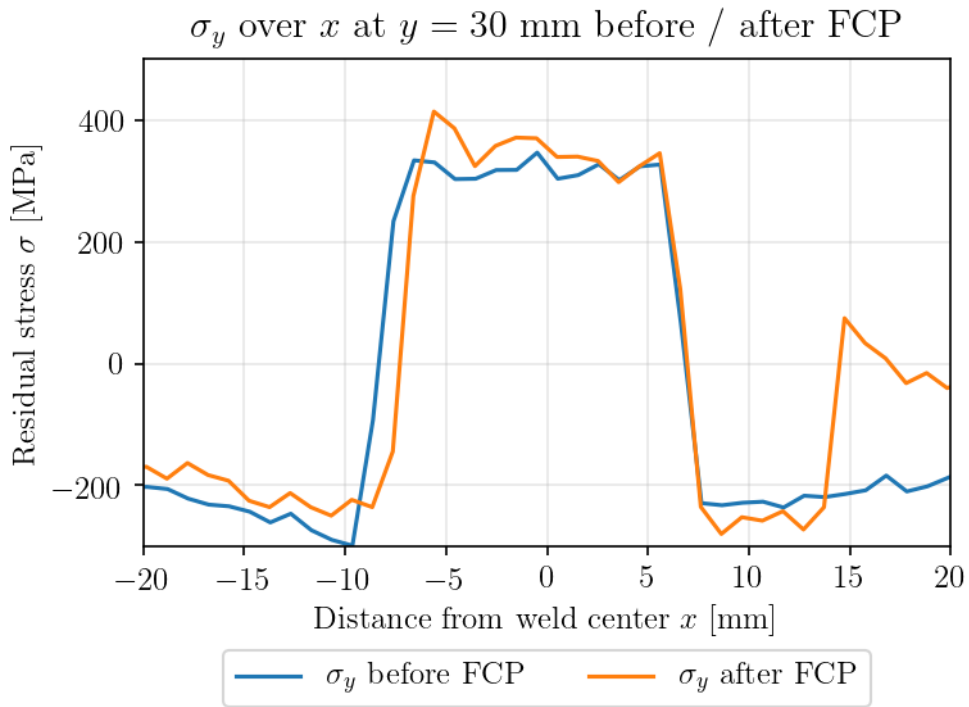
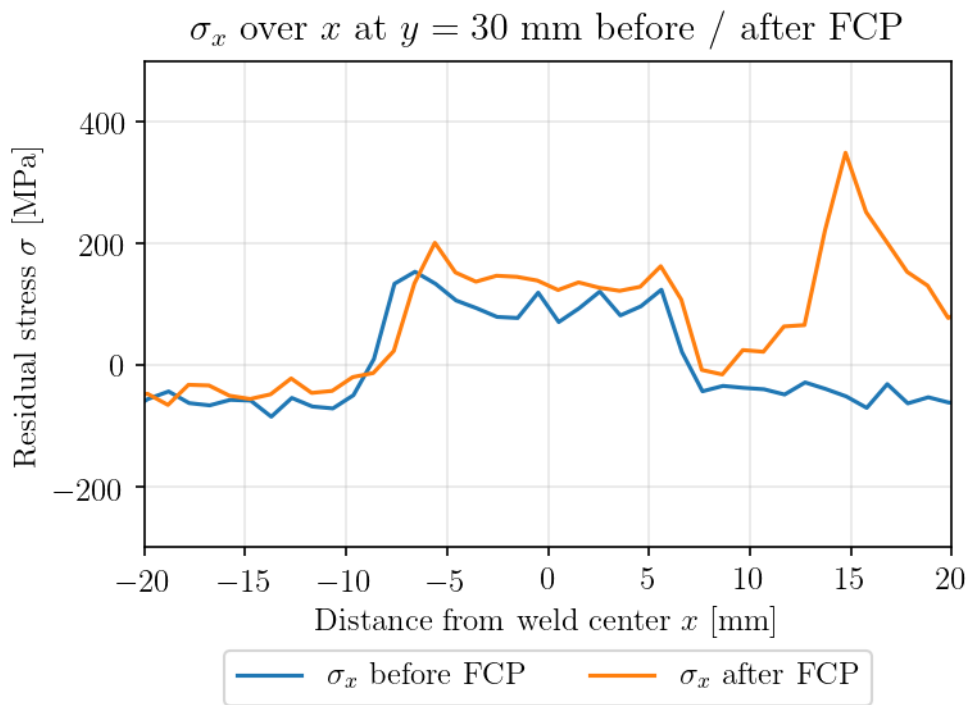


Figure 4.12: a) Transverse and b) Longitudinal RS in a C(T)-100 sample after 4 Mcycles of FCP testing within the scan area indicated in Fig. 4.2.



a)



b)

Figure 4.13: Comparison of the RS state of the C(T) samples before and after crack propagation tests. The selected  $x$  line is at  $y = 30$  mm, where the left crack tip is.

## 4.4 Conclusions

Ti-6Al-4V sheets of 2 mm thickness were coated using the FS process at three different translational speeds. Residual stresses were determined with high-energy X-ray diffraction in transmission geometry. The influence of the residual stress state on the propagation of fatigue cracks perpendicular to the coating line were studied. The following conclusions can be drawn from this study:

1. High-energy X-ray diffraction in transmission geometry yields meaningful results for studying the influence of process parameters on the RS distribution as well as the influence of RS fields on fatigue crack propagation.
2. The FS process, comparable to other welding processes, has an active zone of tensile RS and a compensative zone of induced compressive RS.
3. The stress gradients at the ends of the active zone are very large.
4. RS generated by FS in the longitudinal direction are generally similar in shape and values to the ones generated by FSW, but have higher tensile values in the active zone on the retreating side, while stresses generated by FSW are higher on the advancing side.
5. For the FS process, higher translational speeds show a tendency towards high RS peak values, but the deposited material thickness also influences the resulting RS distribution.
6. Compressive RS generated by the FS process may be the reason for observed fatigue life improvement, that correlates with the RS state. Quantifying this effect requires further investigation.

# Chapter 5

## Residual Stresses in Friction Surfacing Coated AA2024 Sheets

### 5.1 Introduction

**Research topic** The results in the previous chapter have shown that for Ti-6Al-4V coatings on the similar substrate the RS state is affected by the rod translational speed during the deposition. In this chapter the same problem is investigated for Al-based alloys, namely AA5083 and AA6082 deposited on AA2024.

**Materials and process parameters** AA2024 (Al-4.4Cu-1.5Mg-0.6Mn) is a high strength Al alloy that is used extensively in aerospace applications. It is relatively susceptible to localized corrosion in Cl-containing environments as a result of heterogeneous microstructure, hence this investigation is focused on the Friction Surfacing process that deposits alloys of lower strength but higher corrosion resistance on AA2024 sheets. The AA5083 (Al-4.4Mg-0.7Mn-0.15Cr) alloy is a medium-strength, non heat-treatable Al alloy which is generally known for its excellent corrosion resistance. The AA6082 (Si-1.2Mg-0.9Mn-0.6) is an alloy most commonly used for machining. It is a medium-strength structural alloy with excellent corrosion resistance as well.

A comparative study by [Hanke and dos Santos, 2017] presents a review of AA6082 and AA5083 FS deposited coatings on AA2024 substrates. The authors state that

an effective deposition of AA5083 and AA6082 using the same FS parameters can only be done within a limited parameter window. AA5083 is softer and plasticises more easily with heat, so according to [Hanke and dos Santos, 2017] in order to produce thicker coatings it requires lower translational and rotational velocities, and higher axial force. The same axial force and translational velocity applied to AA6082 result in strong vertical growth of the coating and low deposition efficiency. In this investigation of the RS induced by the FS deposition of the two alloys, the axial force and the coating thickness were chosen to be the same as a point of reference, which means that the translational and rotational stud velocities had to be adjusted accordingly for each alloy.

## 5.2 Materials and experimental procedure

**Sample production** FS was carried out using the same machine as described in Section 4.2. However, the deposition of Al alloys was conducted in constant axial force mode, not constant stud consumption mode like for Ti-6Al-4V. The applied process parameters can be found in Table 5.1.

Studs of 20 mm diameter and 120 mm length were used to deposit coatings of approximately 115 mm length on AA2024 sheets of 2–10 mm thickness and 100 mm × 300 mm width and length. An AA2024 sheet of 10 mm thickness was used as backing plate, between the coated substrate and the machine table, in order to enhance the heat dissipation.

Table 5.1: Deposition parameters for AA6082 and AA5083 on AA2024 FS used in this study.

Coating alloy	Rotational vel.	Translational vel.	Axial force
AA5083	1500 min <sup>-1</sup>	4.9 mm/s	9 kN
AA5083	1500 min <sup>-1</sup>	7 mm/s	9 kN
AA5083	1500 min <sup>-1</sup>	10 mm/s	9 kN
AA6082	2000 min <sup>-1</sup>	16 mm/s	9 kN
AA6082	2000 min <sup>-1</sup>	20 mm/s	9 kN
AA6082	2000 min <sup>-1</sup>	24 mm/s	9 kN

Sample production was performed at the department of Solid State Joining Processes of Helmholtz-Zentrum Geesthacht by Stefanie Hanke (Helmholtz-Zentrum Geesthacht, Germany) and Jonas Ehrich (University of Duisburg-Essen, Germany).

**Diffraction measurements** All three types of measurements described in Section 3.1 were performed in this part of the study. In-transmission synchrotron diffraction measurements were performed as line and area scans, geometry shown on Fig. 5.1. In order to determine the  $d_0$  variations in the welded region, stress-free cutouts were made using electrical discharge machining (EDM) as shown on Fig. 5.2 and scanned in transmission the same way the original sheets were.

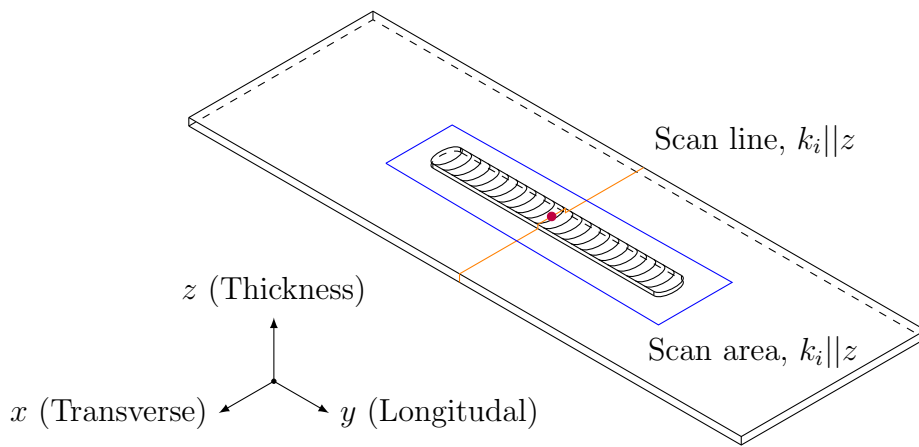


Figure 5.1: Coated sheet geometry and location of the synchrotron beam scan line and scan area.  $k_i$  (incident wave vector) is parallel to  $z$ .

The depth stress state was investigated using synchrotron diffraction with conical slits and angle-dispersive neutron diffraction. Conical slit scans were performed over  $(xz)$  cross-section under the orange line on Fig. 5.1. Neutron diffraction scans were performed over one line parallel to  $z$  axis per sample in the center of the weld, marked by a purple point on Fig. 5.1. Bulk values of the AA2024-T3 elastic constants were used in Hooke's law (Eq. 2.8) and further analysis for in-transmission measurements: elasticity modulus  $E = 71.0$  GPa, Poisson number  $\nu = 0.33$ , yield strength  $\sigma_{yield} = 345$  MPa [Boyer and Gall, 1985]. For the neutron diffraction analysis of the AA6082 coating elastic constants of AA6082-T4 were used:  $E = 70.0$  GPa, Poisson number  $\nu = 0.33$  [Boyer and Gall, 1985].

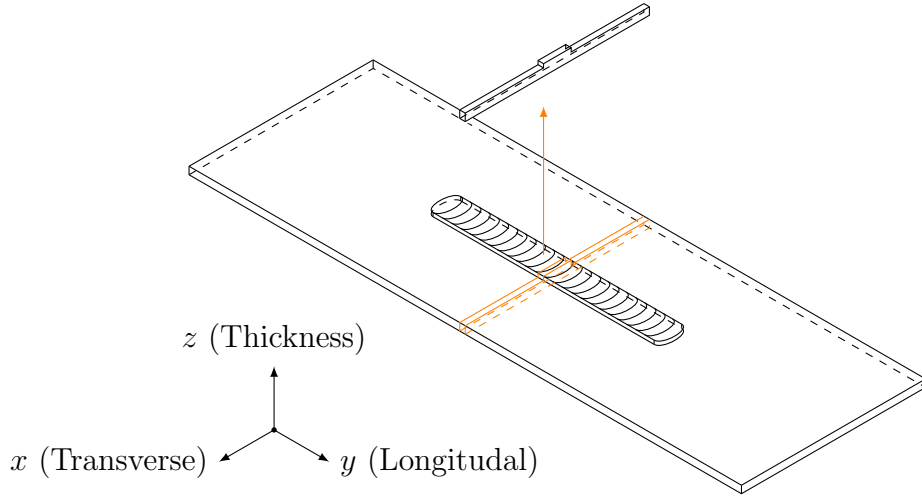


Figure 5.2: FS coated sheet and reference cutout geometry. For all synchrotron experiments  $k_i$  (incident wave vector) was parallel to  $z$ . Cutout size in  $y$  direction is 1 mm.

### 5.3 Results and discussion

**Comparison of AA6082 and AA5083 coatings** According to [Hanke and dos Santos, 2017], the heat input in the substrate is smaller for AA5083 than for AA6082 at the same deposition parameters. But in this investigation the translational speed for AA5083 is 1.6–4.9 times lower, which leads to higher heat input into the substrate. This is the possible explanation for the difference we see in the RS states for the two coating alloys (Figs. 5.3 and 5.5 for  $\sigma_y$ , Figs. 5.4 and 5.6 for  $\sigma_x$ ). Higher heat input of AA5083 (Fig. 5.3) leads to the substrate being more heated and more plasticized, hence the common for welding processes M-shape in longitudinal stresses, while in AA6082 (Fig. 5.5) coatings there is no M-shape and the overall RS values are higher.

The results show that the AA2024 sheets had RS prior to deposition. This is especially visible on Fig. 5.5, where the  $\simeq 40$  MPa difference between longitudinal and transverse stresses is present everywhere outside of the coating. These RS likely come from the rolling during the sheet production, and their effect on the RS induced by the coating deposition has not been investigated.

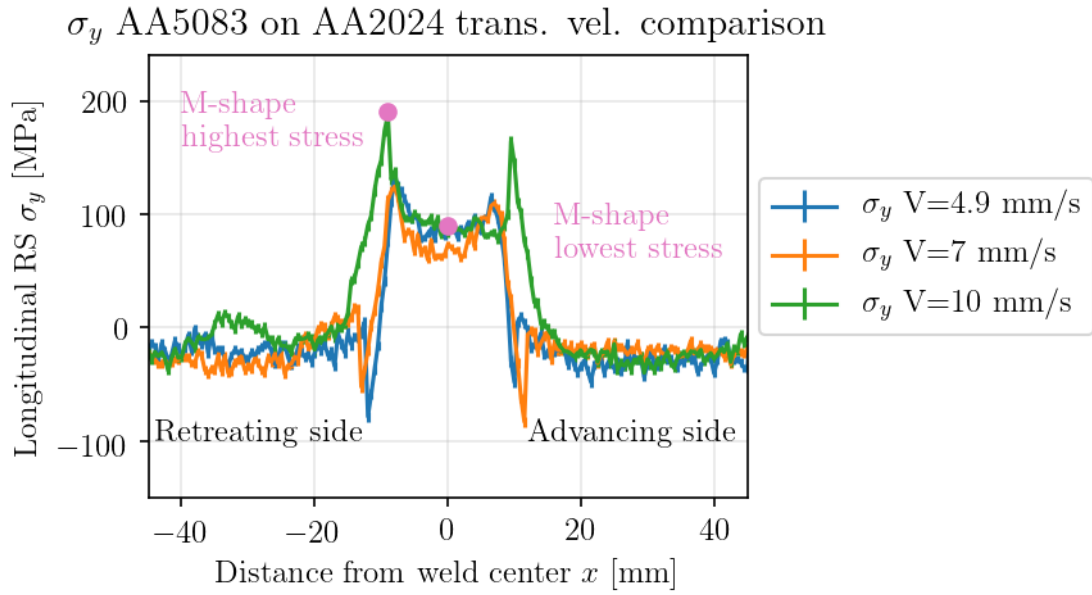


Figure 5.3: Longitudinal  $\sigma_y$  RS distribution along the scan line after coating deposition as determined from X-ray diffraction in transmission geometry.

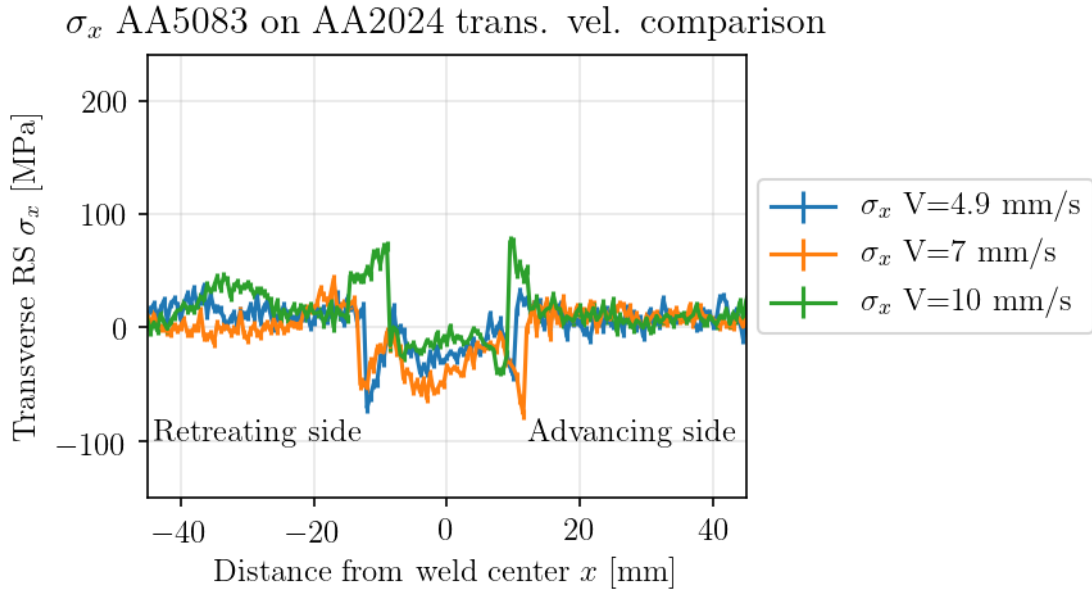


Figure 5.4: Transverse  $\sigma_x$  RS distribution along the scan line after coating deposition as determined from X-ray diffraction in transmission geometry.

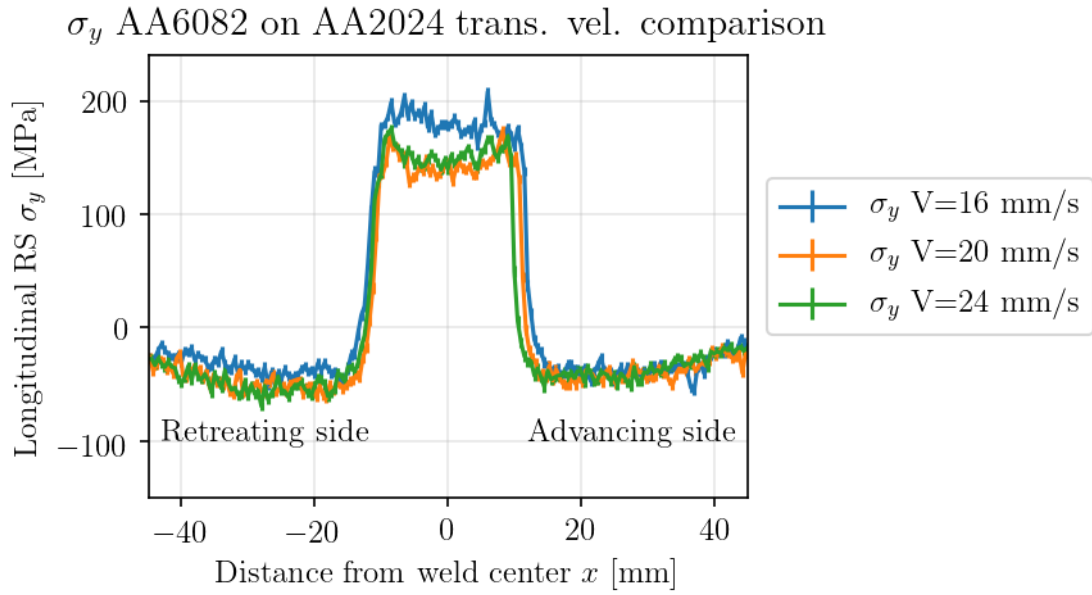


Figure 5.5: Longitudinal  $\sigma_y$  RS distribution along the scan line after coating deposition as determined from X-ray diffraction in transmission geometry.

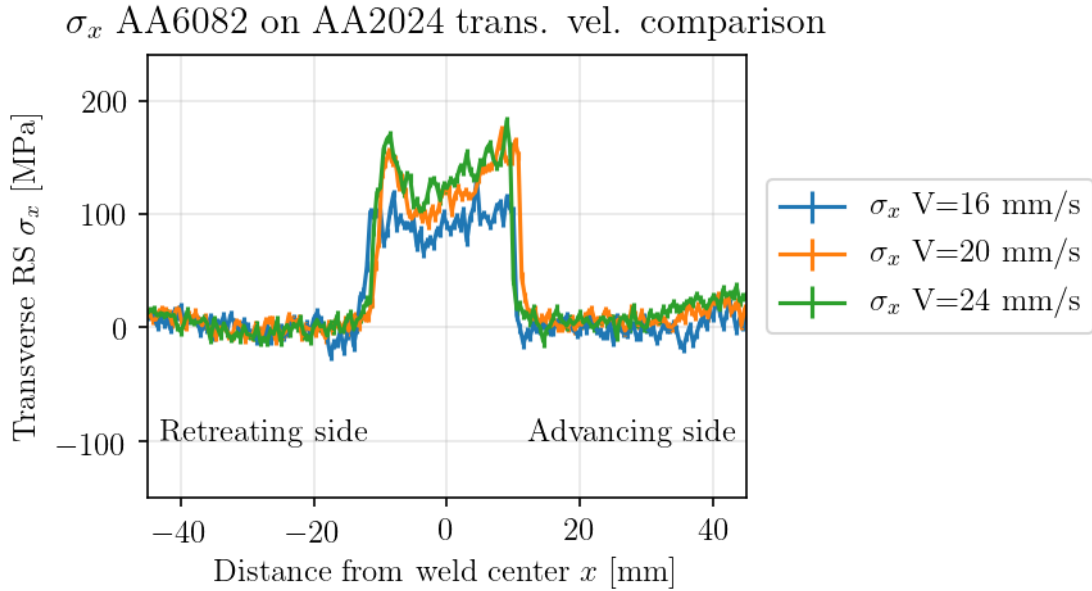


Figure 5.6: Transverse  $\sigma_x$  RS distribution along the scan line after coating deposition as determined from X-ray diffraction in transmission geometry.

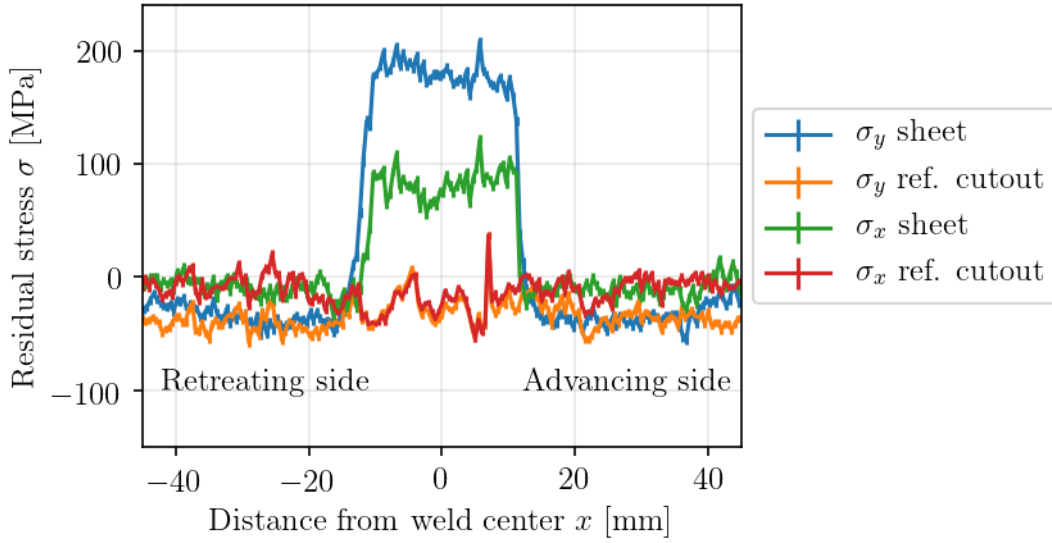
**AA5083 translational velocity dependence** In AA5083 coatings the proportion of the highest to lowest tensile stresses in the M-shape (see markings on Fig. 5.3 for the 10 mm/s line) grows with the translational velocity: 1.55, 1.75, 2.07 for 4.9, 7, 10 mm/s respectively. This could be due to more heat input leading to more plastification and / or thermal softening under the coating, hence more material relaxation and less pronounced M-shape peaks.

**AA6082 translational velocity dependence** AA6082 RS distributions, unlike both Ti-6Al-4V and AA5083, have no M-shape and no obvious trend between the translational velocity and stress amplitude. The tensile stresses in the coated area are uniform and similar in value to peak AA5083 stresses. The lower (compared to AA5083) heat input during the AA6082 deposition produces the tensile RS, but no relaxation in the mid region, hence no M-shape. The lack of difference in the RS states between 16, 20, 24 mm/s translational velocities comes from the heat input being almost the same, which will be discussed in more detail in the following chapter.

**Reference measurements** In order to see if there are any  $d_0$  changes in the coated region, 2 mm wide cutouts were made (scheme on Fig. 5.2) from the coated sheets and line stress scans were performed on them. Fig. 5.7 shows a comparison between the stress states of one of the samples with its reference cutout a) for AA6082 on AA2024 coatings and b) for AA5083 on AA2024 coatings. The plots show that there are no significant changes in the coated region and  $d_0$  can be assumed constant along the whole sample.

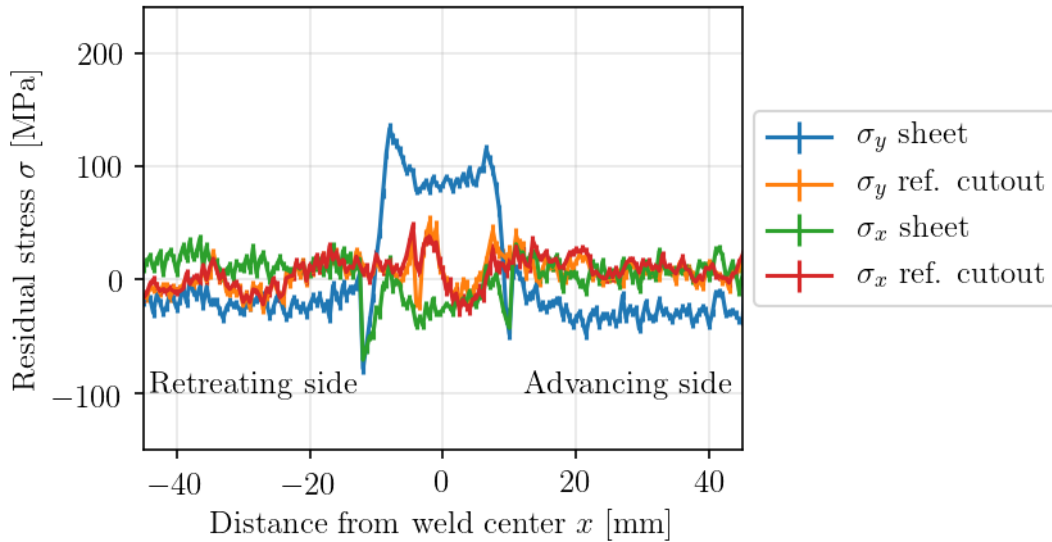
Additionally, Fig. 5.7 a) shows that for the reference cutout of the AA6082 weld,  $\sigma_x$  and  $\sigma_y$  lines fall together in the welded region. This indicates relaxation of the substrate microstresses due to thermal treatment. For the AA5083 weld cutout on Fig 5.7 b), the  $\sigma_x$  and  $\sigma_y$  lines fall together along the whole cross-section. Due to the higher heat input of the AA5083 FS deposition, the microstresses have relaxed below and around the welded zone.

AA6082 on AA2024 2mm thick substrate,  
Tr. vel. 16 mm/s



a)

AA5083 on AA2024 2mm thick substrate  
Tr. vel. 4.9 mm/s



b)

Figure 5.7: Comparison of longitudinal  $\sigma_y$  and transverse  $\sigma_x$  RS distribution for a FS coated sheet and its  $d_0$  reference. a) AA6082 on AA2024, b) AA5083 on AA2024.

**AA6082 machining the coating** The coatings produced by the FS have an irregular shape and a rough surface, so for the process to be used in production, the coating surface needs to be machined after the deposition. Figs. 5.8 a) and b), where the same FS coated sample was scanned for RS before and after machining its  $\simeq 2.2$  mm thick coating down to 1 mm, show that removing part of the coating has little effect on the RS state.

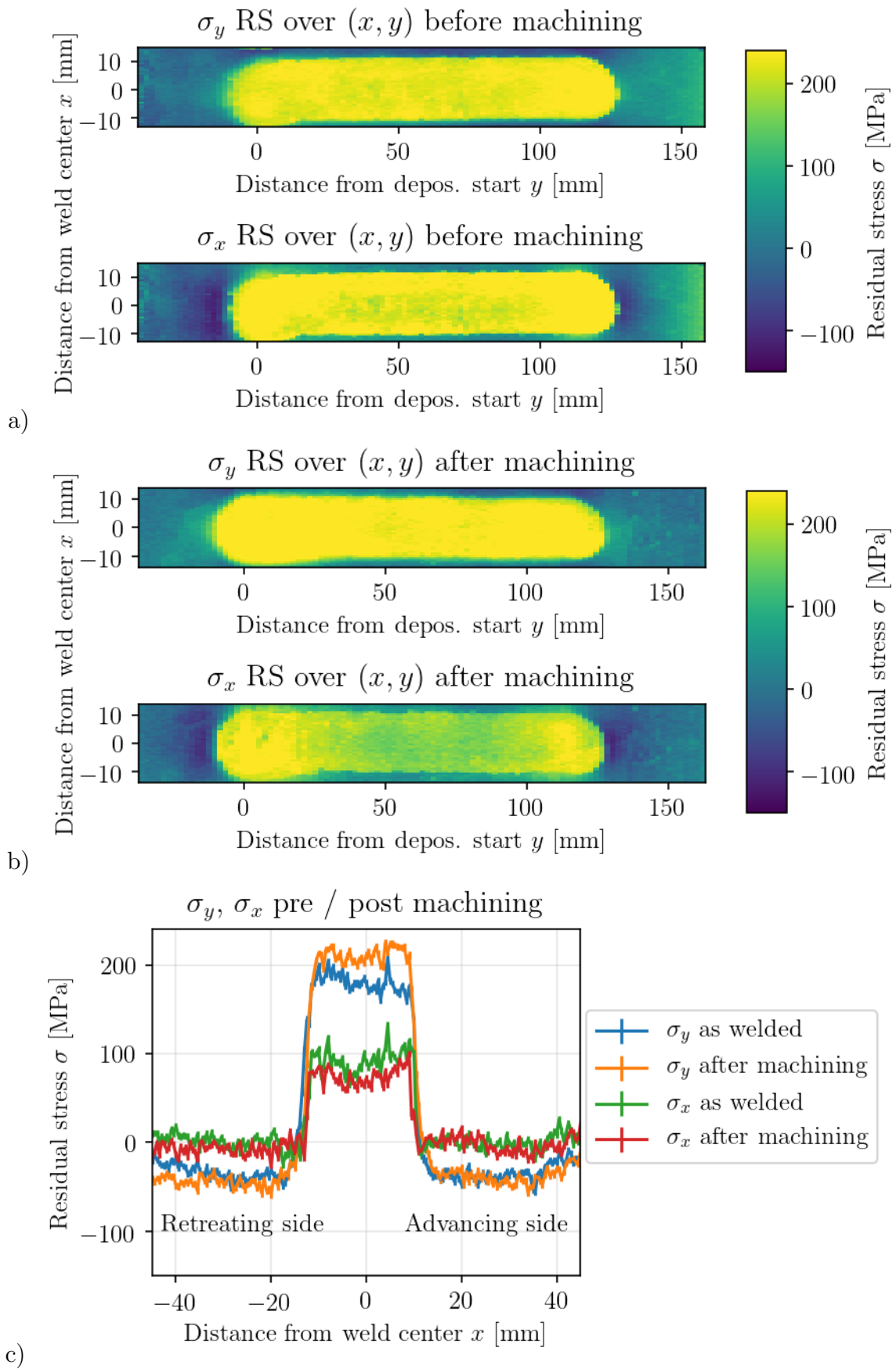


Figure 5.8: AA6082 on AA2024 longitudinal  $\sigma_y$  and transverse  $\sigma_x$  RS in the coated area and around it as measured by X-ray in transmission geometry. a) As welded b) Machined to 1 mm thickness. c) comparison of the as welded / machined line scans.

The difference in RS state induced by the machining is only visible at a closer look on Fig. 5.8 c). After machining there is a slight increase in  $\sigma_y$  and a slight decrease in  $\sigma_x$ . The reason for this discrepancy will become clear when looking at the neutron depth RS distributions in the following paragraph.

**AA6082 coating-substrate stress distribution** The fact that the RS state of the coated sheet changes very little after machining the coating is further supported by the depth RS distributions. The RS scans along the  $z$  axis obtained by neutron diffraction on Fig. 5.9 show that for any substrate thickness most of the tensile stresses induced by FS are in the substrate, while in the coating the RS amplitude is lower. The top left image on Fig. 5.9 shows the depth RS distribution of the same sheet that was scanned for Fig. 5.8 a), c). The top left depth scan on Fig. 5.9 shows that after removing some of the coating material the average value of  $\sigma_y$  should slightly increase, and of  $\sigma_x$  should slightly decrease.

Most RS are concentrated in the substrate possibly due to the lack of constraining conditions on the coating during its cooling: since it is only connected to the substrate from one side, the material in it is more free to move. It is known, however, that in some cases (for example if there was a thick oxide layer on the substrate before deposition) part of the coating delaminates during cooling, so the RS in the bonding region and the coating can not be disregarded completely.

The progression of the images on Fig. 5.9 shows depth RS distributions for FS coatings deposited with the same parameters on 2 – 10 mm thick substrates. It is clear that the thicker the substrate is, the more developed the compensative zone with the compressive stresses becomes. A 2 mm thick substrate can only develop tensile stresses below the coating, with the compensative zone being around the coated area. A 6 mm and more thick substrates have part of the compensative zone below the coating, starting at 4 – 5 mm deep.

The  $xz$  cross-section RS scan by synchrotron radiation with conical slits of a 4 mm thick sample on Fig. 5.10 shows a similar picture to the neutron line scans. These two methods independently give very close RS values at the same position in the sample. From the 2D scans one can see that the active zone with the tensile stresses

forms directly below the coating and has approximately the same width, while the compressive stresses concentrate on the bottom of the substrate.

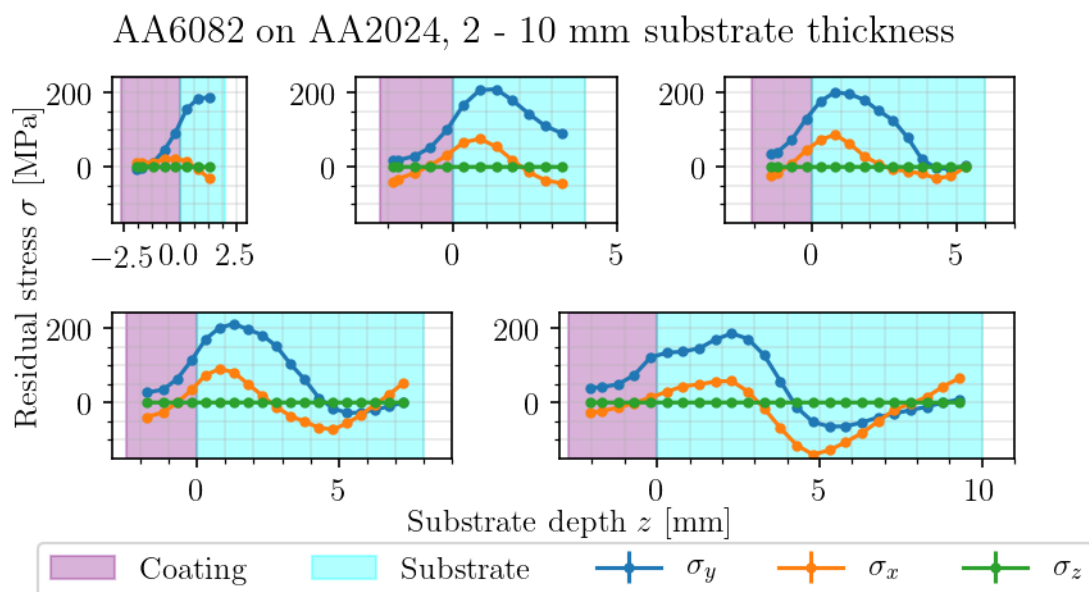


Figure 5.9: RS distributions as measured by neutron diffraction for different substrate sheet thicknesses.  $\sigma_z$  is 0 due to the plane stress condition. Mean error is  $\delta\sigma \simeq 10$  MPa, so the errorbars are not clearly visible.

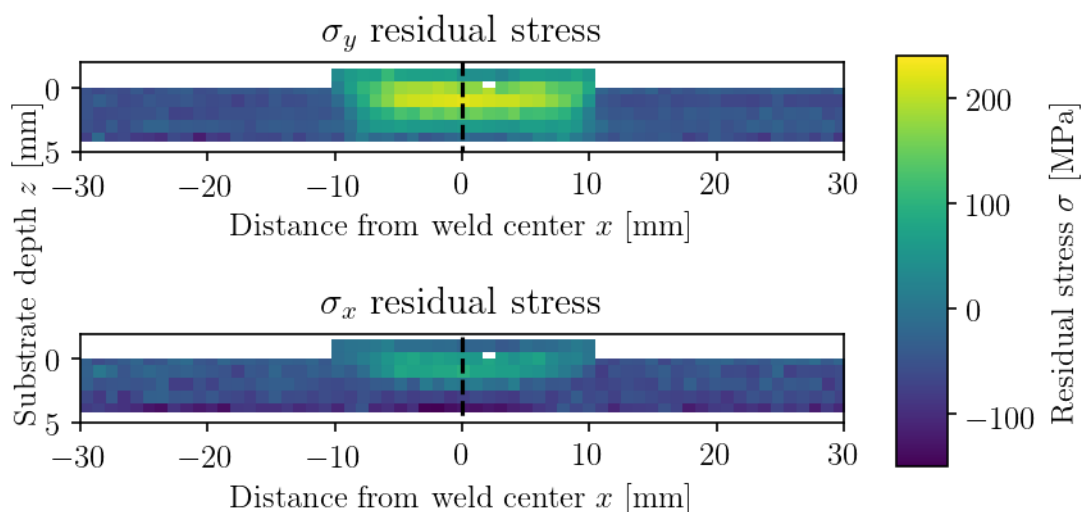


Figure 5.10: Longitudinal  $\sigma_y$  and transverse  $\sigma_x$  RS over  $xz$  cross-section as measured by X-ray diffraction with a conical slit cell.

## 5.4 Conclusions

1. The general shape of RS distributions for Al-based alloys is similar to the Ti-6Al-4V, however the tensile stresses in Al are higher relative to the yield stress: maximum of 58% yield stress for AA2024 vs. 44% yield stress for Ti-6Al-4V.
2. AA6082 and AA5083 FS coatings on AA2024 substrate show similar maximal tensile stress values of  $\sim 180$  MPa (58% yield stress).
3. AA6082 and AA5083 FS coatings on AA2024 substrate show different stress profile shapes: AA5083 RS are M-shaped, and AA6082 are not. The difference possibly comes from AA5083 deposition being much slower with larger heat input and more substrate softening.
4. Deposition of both AA6082 and AA5083 coatings produces no changes in  $d_0$  value in the AA2024 substrate.
5. In AA6082 coatings on AA2024 substrates the tensile RS are mostly concentrated in the substrate, not the coating.
6. The RS in the substrate below the coating are tensile for 2 – 4 mm substrates over the whole substrate thickness. For 6 – 10 mm thick substrates the RS distribution has an active zone right below the coating, and then a compensative zone starting at  $\sim 4$  mm deep.
7. Machining half of the thickness of the AA6082 coating produces only a small effect (less than 10%  $\sigma_x$  decrease and  $\sigma_y$  increase) on the RS state, because the stresses are mostly concentrated in the substrate.
8. Tensile stresses induced by the FS deposition form in the substrate right below the coating, and the compressive stresses concentrate on the opposite to the coating side of the substrate.

# Chapter 6

## Deposition efficiency of Friction Surfacing on AA2024 Sheets

### 6.1 Introduction

**Research topic** The previous chapter that investigated the connection between various FS deposition parameters and the RS state of the coated sheets has posed an important question: why do the stress states of different welds look so similar? There is little change in the RS state between investigated translational velocities for AA6082 on AA2024, and the coating-substrate depth stress distributions for different substrate thicknesses look almost like the same function cut at different intervals (Fig. 5.9). In order to understand the reason for these similarities, an investigation into the temperature regime during the AA6082 on AA2024 deposition was performed.

In this chapter the connection between heat dissipation and deposition efficiency is investigated for AA6082 on AA2024 FS welds. Multiple depositions were performed at different temperature ranges, with temperature data collected from the bottoms of the substrates to avoid influencing the process. The temperature data was then used in a FEM model to estimate the heat input into the substrate for each deposition. To change the process temperature range without changing FS parameters, heat-dissipating (Al) and heat-insulating (Ti) backing plates were used, as well as cooling the substrate and the backing plate prior to the deposition. The results have

shown a correlation between the heat input and the deposition efficiency, with starting substrate temperature as an additional parameter.

**Literature overview** Several studies in which no special cooling equipment was used have reported that the deposition efficiency increases with a decrease of the heat input. [Sakihama et al., 2003] report increasing efficiency with increasing translational stud speed and decreasing efficiency with increasing axial force and rotational speed for AA5052 alloy. [Galvis et al., 2017] also report an increase in efficiency coming from an increase in translational stud speed for depositing AA6351 on AA5052. Additionally, a study by [Li and Shinoda, 2013] has reported a significant increase in deposition efficiency compared to passive air cooling if FS of stainless steel was carried out in a cooling water bath. [Li and Shinoda, 2013] note the negative correlation between the deposition efficiency and the heat generation without the water bath as well.

Put together, these studies lead to a hypothesis that the heating power of the depositing rod during the process is larger than what can be dissipated by passive air cooling. To put it another way, with nothing but air cooling FS deposition of Al and possibly other materials does not work at its maximum efficiency. The purpose of the current investigation is to develop and test this hypothesis.

## 6.2 Experimental and numerical procedure

**Sample production** FS was carried out on the same machine as described in Section 4.2 in constant axial force mode. In order to see the effects of heat dissipation on deposition efficiency, five sets of welds (22 welds total) were made. First three sets started at room temperature and were passively air cooled. They had a 10 mm thick Al plate, a 10 mm thick Ti plate, or a KlingerSil C-4400 sheet (thermal conductivity 121.0, 6.7, and 0.42 W/m · K respectively) as backing plates. Next two sets used the same Al or Ti backing plates, but both substrate and backing plate were submerged in liquid nitrogen (LN<sub>2</sub>) prior to the deposition, until the TC mounted as shown on Fig. 3.8 registered  $-120^{\circ}$  C. Within each set several welds were performed on substrates

of 2 – 10 mm thickness, deposition parameters can be found in Table 6.1.

Table 6.1: Deposition parameters for the efficiency study. Translational velocity was 16 mm/s, rotational velocity 2000 min<sup>-1</sup>, axial force 9 kN.

Backing plate	Substrate	Starting $T$
10 mm AA2024	2 mm AA2024	22°C
10 mm AA2024	4 mm AA2024	22°C
10 mm AA2024	6 mm AA2024	22°C
10 mm AA2024	8 mm AA2024	22°C
10 mm AA2024	10 mm AA2024	22°C
10 mm Ti-6Al-4V	2 mm AA2024	22°C
10 mm Ti-6Al-4V	4 mm AA2024	22°C
10 mm Ti-6Al-4V	6 mm AA2024	22°C
10 mm Ti-6Al-4V	8 mm AA2024	22°C
10 mm Ti-6Al-4V	10 mm AA2024	22°C
2 mm KS C-4400	2 mm AA2024	22°C
2 mm KS C-4400	4 mm AA2024	22°C
2 mm KS C-4400	6 mm AA2024	22°C
2 mm KS C-4400	8 mm AA2024	22°C
2 mm KS C-4400	10 mm AA2024	22°C
10 mm AA2024	2 mm AA2024	-120°C
10 mm AA2024	4 mm AA2024	-120°C
10 mm AA2024	8 mm AA2024	-120°C
10 mm AA2024	10 mm AA2024	-120°C
10 mm Ti-6Al-4V	2 mm AA2024	-120°C
10 mm Ti-6Al-4V	4 mm AA2024	-120°C
10 mm Ti-6Al-4V	8 mm AA2024	-120°C

For the study of the effect of the translational velocity on deposition efficiency and thermal conditions during the deposition, six additional welds were made, parameters shown in Table 6.2. Substrates and backing plates were mounted on a room temperature steel machine table with a heat isolating coating. During the deposition the temperatures were measured as described in Section 3.3. Deposition efficiency for each weld was calculated from used studs length and mass using Eq. 2.4.

Table 6.2: Deposition parameters for the translational velocity effect study. Rotational velocity was  $2000 \text{ min}^{-1}$ , axial force 9 kN.

Backing plate	Substrate	Starting $T$	Translational vel.
10 mm AA2024	2 mm AA2024	22°C	16 mm/s
10 mm AA2024	2 mm AA2024	22°C	20 mm/s
10 mm AA2024	2 mm AA2024	22°C	24 mm/s
10 mm AA2024	4 mm AA2024	22°C	16 mm/s
10 mm AA2024	4 mm AA2024	22°C	20 mm/s
10 mm AA2024	4 mm AA2024	22°C	24 mm/s

Sample production was performed at the department of Solid State Joining Processes of Helmholtz-Zentrum Geesthacht with the help of Arne Roos (Helmholtz-Zentrum Geesthacht) and Jonas Ehrich (University of Duisburg-Essen, Germany).

**Heat propagation modeling** Wolfram Mathematica 11 Student Edition by [Wolfram Research Inc., 2018] was used to perform the setup and computation of a heat propagation model. At the root of the model was the heat equation in the form of

$$\partial_t T(x, z, t) - \alpha \Delta T(x, z, t) = h(x, z, t), \quad (x, z) \in \Omega. \quad (6.1)$$

Eq. 6.1 was solved over a 2D domain  $\Omega$  representing an  $xz$  cross-section of the sample and its backing plate (Fig. 6.1). In it  $x, z$  are space coordinates,  $t$  is time,  $T$  represents the temperature field,  $\alpha$  is the thermal diffusivity constant specific for each material, and  $h$  is the heater function.

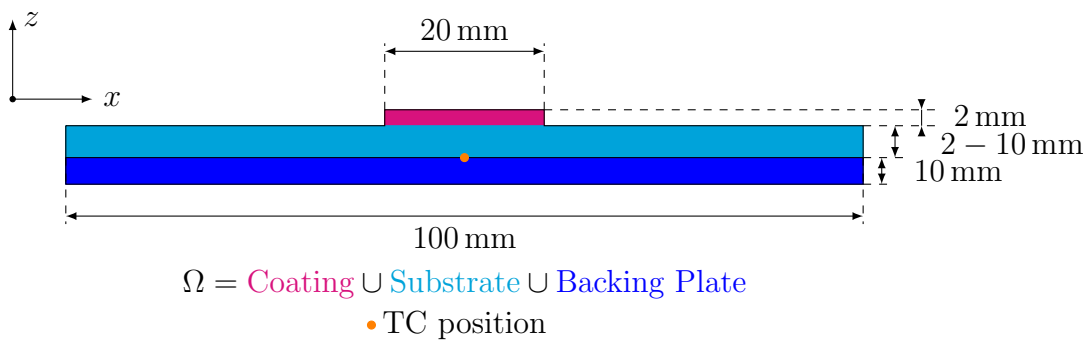


Figure 6.1: Scheme of the heat propagation model domain.

A 2D model of a 3D process is a significant simplification. However, as the FS process reaches a steady state, one can argue that every  $xz$  cross-section experiences the same thermal conditions as the depositing rod passes over it, so the simplification is appropriate.

The part of the domain  $\Omega$  representing the coating was a volumetric heat source, whose heating power  $h(t)$  changed over time corresponding to the real heat source passing along the  $xz$  slice. Hence, the  $h(x, z, t)$  function in Eq. 6.1 takes the form

$$h(x, z, t) = \begin{cases} h(t) & \text{if } (x, z) \in \text{Coating} \\ 0 & \text{if } (x, z) \in \text{Substrate} \cup \text{Backing Plate} \end{cases} \quad (6.2)$$

Boundary conditions were set to restrict the heat flow over the sample border

$$(\mathbf{n}, \nabla) T(x, z, t) = 0, \quad (x, z) \in \partial\Omega, \quad (6.3)$$

and the initial conditions were set as

$$T(x, z, t) = T_0, \quad t = 0. \quad (6.4)$$

By solving Eqns. 6.1 - 6.4 one can determine the temperature field and its evolution over time  $T(x, z, t)$  for any given heater function  $h(t)$ .

The values for the thermal diffusivity  $\alpha$  were calculated from the material properties: thermal conductivity  $K$ , specific heat capacity  $C_p$ , and density  $\rho$

$$\alpha = \frac{K}{C_p \cdot \rho}. \quad (6.5)$$

Table 6.3: Thermal properties of the alloys used in the study [Boyer and Gall, 1985].

Material	$K$ [W/m · K]	$C_p$ [J/kg · K]	$\rho$ [kg/m <sup>3</sup> ]	$\alpha$ [m <sup>2</sup> /s]
AA2024, AA6082	121.0	875.0	2780.0	$4.97 \cdot 10^{-5}$
Ti-6Al-4V	6.7	526.0	4430.0	$2.88 \cdot 10^{-6}$

The task at hand was to estimate  $h(t)$ , knowing the cross-section geometry and the  $T(x_0, y_0, t)$  data for one point inside the domain  $(x_0, y_0) \in \Omega$  as measured by TC experiments. There is no ambiguity in the solution: with a specified geometry and boundary conditions, for any given  $T(x_0, y_0, t)$  there is only one  $h(t)$  function. However, there is no direct way to calculate  $h(t)$ : the equation can only be solved for

$T(x, z, t)$  given a specific  $h(t)$ . Hence, successive approximations of the heater function  $h(t)$  were used in order to fit the TC data with the simulated  $T$  field.

Successive approximations were done by hand with the visual fit quality control. An automated fitting procedure would be more reliable, but it would require significant computing power and a costly additional license for using it. The fits obtained by hand agree with the TC data enough to draw conclusions about the heat input, which is the main point of this investigation.

## 6.3 Results and discussion

**Deposition efficiency** The first set of FS coating depositions was performed on 2–10 mm thick substrates with a 10 mm thick Al backing plate. Deposition efficiency does not change significantly between these samples (blue line on Fig. 6.2). However, when a heat isolating (Ti and Klinger Sil show similar enough results to make no distinction between them) backing plate was used, on a 2 mm thick substrate the FS did not work (see a picture of the coating on Fig. 6.3), and on thicker substrates deposition efficiency grew proportionally to the substrate thickness (orange and purple lines on Fig. 6.2), at 10 mm reaching a value close to the efficiency with the Al backing plate.

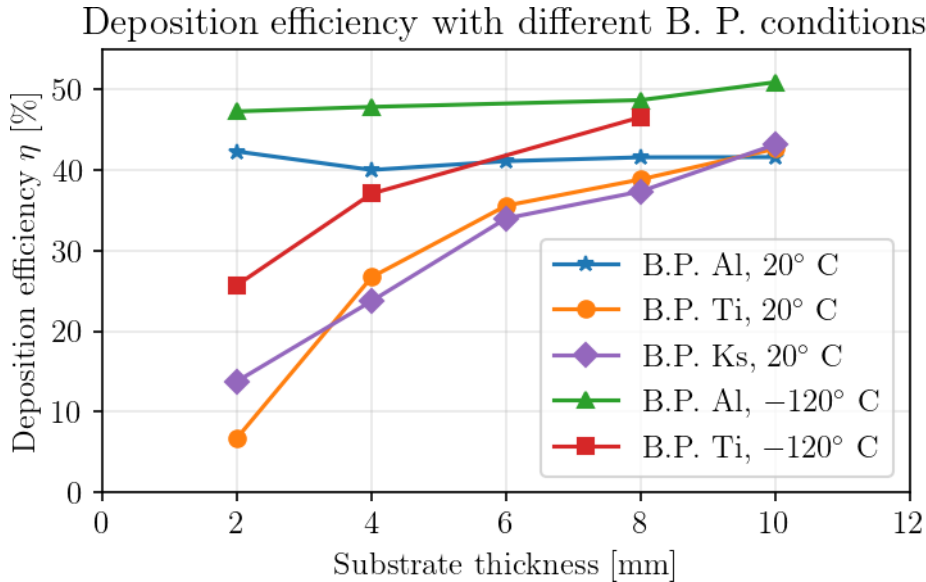


Figure 6.2: Deposition efficiency for various substrate thicknesses at two starting substrate temperatures: raw experimental data.

For the next set of FS depositions, substrates and backing plates were cooled to  $-120^{\circ}\text{C}$  by submerging in a  $\text{LN}_2$  bath prior to the deposition. This has yielded a consistent 8–10% increase in deposition efficiency for both Al and Ti backing plates (green and red lines on Fig. 6.2 respectively).

First of all, these results suggest that the heat conductivity from the substrate to the Al backing plate is not impaired by the border between them. If it were, the changes between the different substrate thicknesses on an Al backing plate would be noticeable. Hence, the substrate and the Al backing plate effectively form a thicker

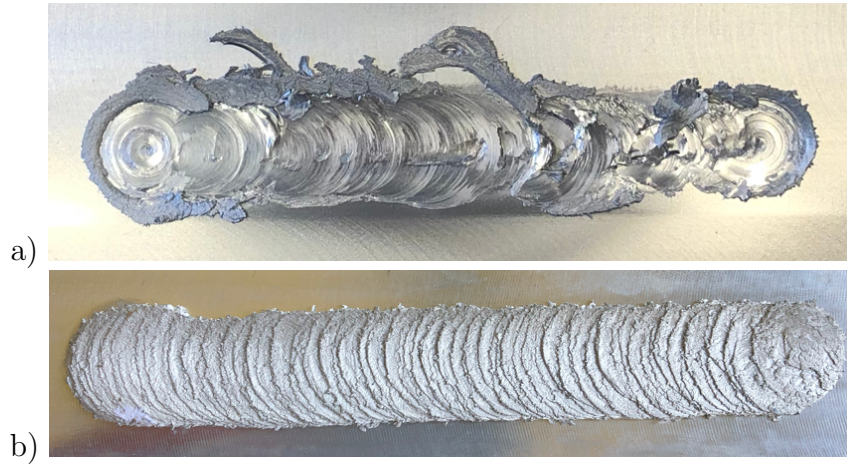


Figure 6.3: Photos of coatings deposited on 2 mm thick substrates a) with a Ti backing plate b) with an Al backing plate.

substrate with the heat isolating machine table below, for both pre-cooled and room temperature sets. This means, Fig. 6.2 can be redrawn in a more clear manner, which is Fig. 6.4. There the thickness of the Al backing plate is just added to the thickness of the substrate, hence 2 mm substrate on 10 mm Al backing plate is considered 12 mm substrate, 4 mm substrate on 10 mm Al backing plate is 14 mm, and so on.

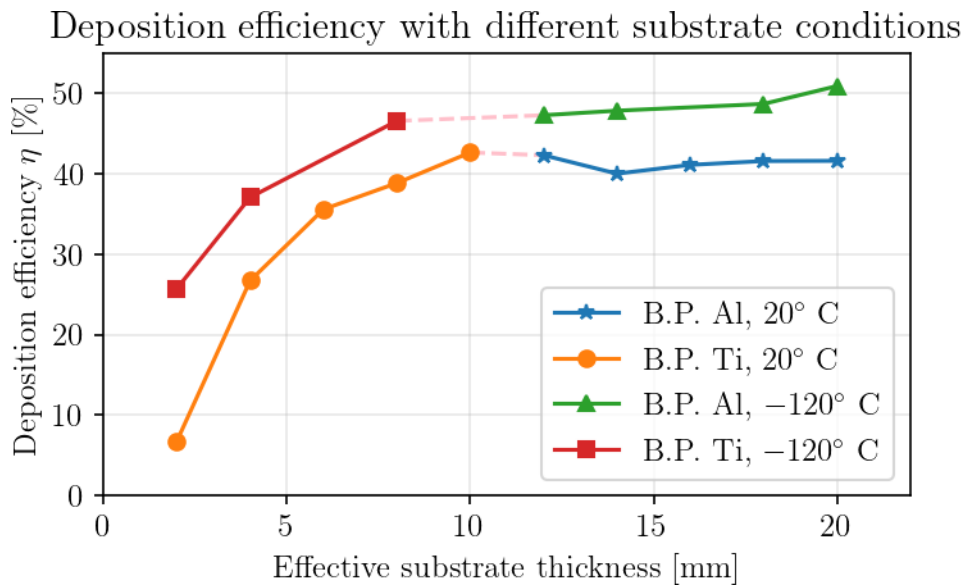


Figure 6.4: Deposition efficiency vs. effective substrate thickness (substrate + backing plate thickness if the backing plate is Al, or just the substrate thickness if the backing plate is heat isolating) for two starting substrate temperatures: 20° C and -120° C. The estimated error in deposition efficiency is  $\delta\eta = \pm 4\%$ .

Fig. 6.4 looks as if for each starting temperature the deposition efficiency grows with the substrate thickness when there is less than 10 mm of substrate, then reaches saturation and stays at the same value for 10 – 20 mm thick substrates. A consistent increase in efficiency at any substrate thickness when starting at a lower temperature suggests that the efficiency depends on the amount of heat the substrate can accept from the depositing rod while staying in the temperature window allowing the bonding of the coating to happen.

**Model fit of the temperature data** The 2D heat propagation model was used to evaluate the temperature data collected during coating deposition. The model has proven to be valid by correctly estimating the heating and cooling rates for all investigated cases. Experimental temperature data and the fitting model curves are presented on Figs. 6.5 - 6.8. The cooling rates for Al backing plate at room temperature (Fig. 6.5) are a very close fit. Apart from general applicability of the model, this proves that the boundary conditions restricting heat flow (Eq. 6.3) were chosen correctly. It shows that the material cooling immediately after the deposition happens due to substrate material self-equilibrating. For the rest of the sample sets the fit is not as good as for the Al backing plate at room temperature, but the quality is enough to estimate the heat input, since the maximum  $T$  and heating times between the model and the experiment are close.

For the case of Ti backing plates, a modification was introduced into the model. The thermocouples positioned at the material boundary are a complication since it is not clear, how being unevenly surrounded by two materials of different heat conductivity and temperature affects the temperature readings. To account for that, the temperature in the FEM model to fit the TC data was taken not from the material boundary, but 0.3 mm deep into the Ti backing plate. The value of 0.3 mm has been found as a best fitting parameter in an optimization procedure and is a reasonable value from the experimental perspective.

Al backing plate, deposition at room temperature

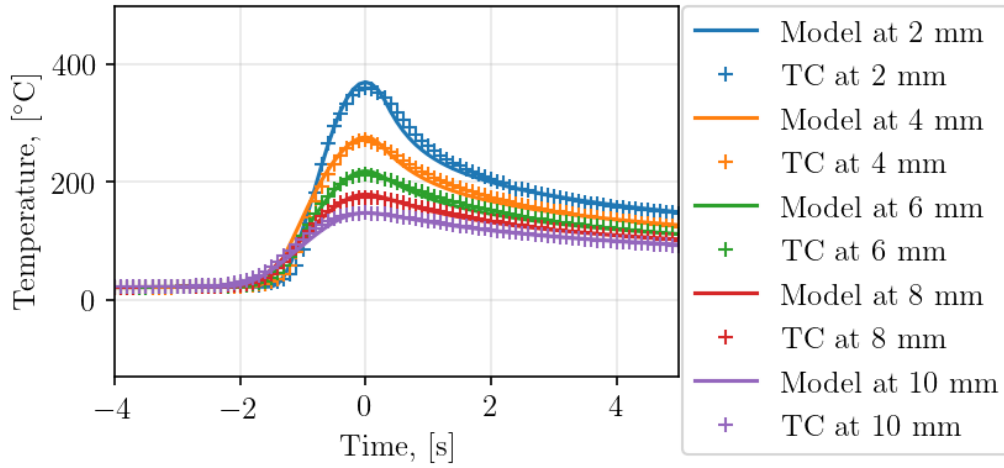


Figure 6.5: TC measurements and heat propagation model fits for AA6082 on AA2024 deposition on Al backing plate starting at room temperature.

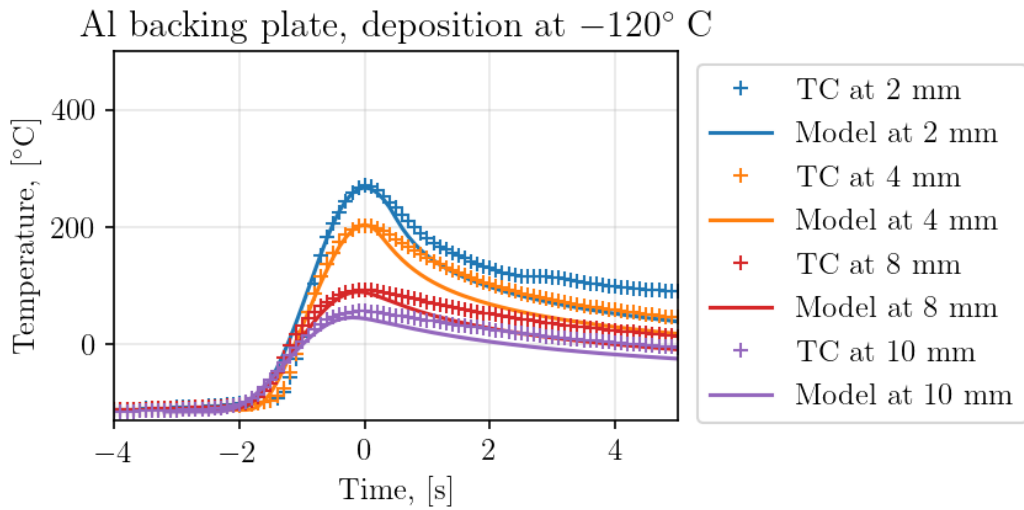


Figure 6.6: TC measurements and heat propagation model fits for AA6082 on AA2024 deposition on Al backing plate starting at room -120°C.

Ti backing plate, deposition at room temperature

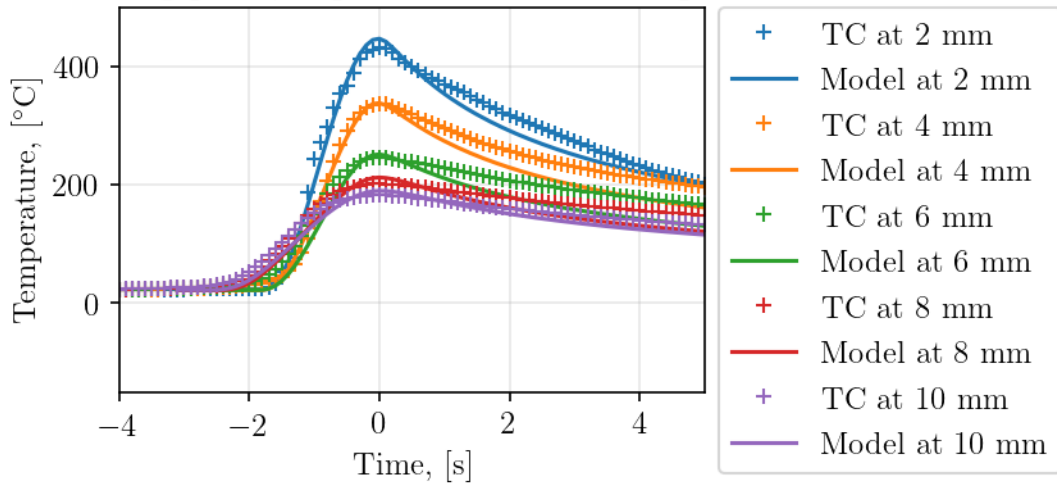


Figure 6.7: TC measurements and heat propagation model fits for AA6082 on AA2024 deposition on Ti backing plate starting at room temperature.

Ti backing plate, deposition at  $-120^{\circ}\text{C}$

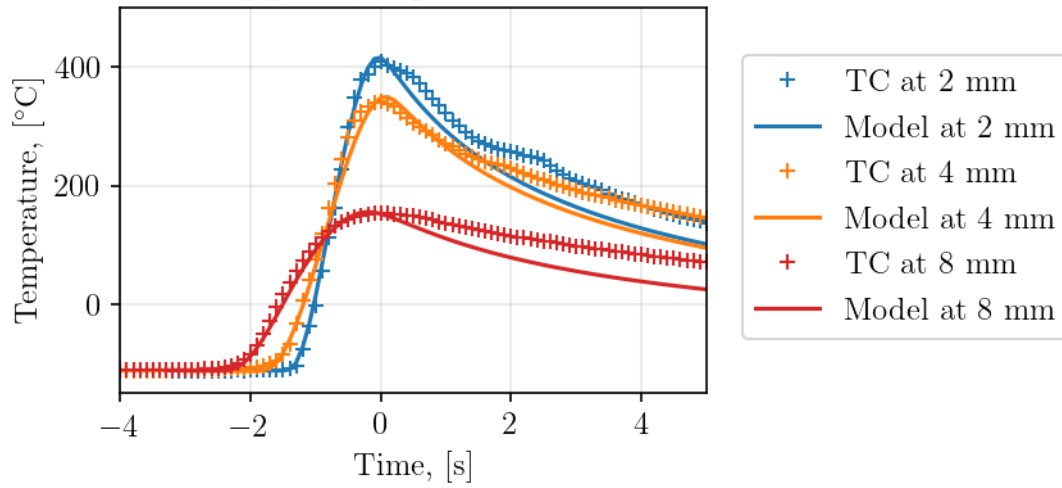


Figure 6.8: TC measurements and heat propagation model fits for AA6082 on AA2024 deposition on Ti backing plate starting at room  $-120^{\circ}\text{C}$ .

**Model heat input vs. deposition efficiency** The relation between the heat input calculated via FEM modelling and the effective substrate thickness is shown on Fig. 6.9. The general similarity between this plot and Fig. 6.4 is noticeable: same as the deposition efficiency on Fig. 6.4, the heat input on Fig. 6.9 increases with the substrate thickness increase until at 10 mm thickness a saturation value is reached. The heat inputs for the two starting temperatures (orange and blue vs red and green lines on Fig. 6.9) follow similar trends with different absolute values, similar to the deposition efficiency on Fig. 6.4.

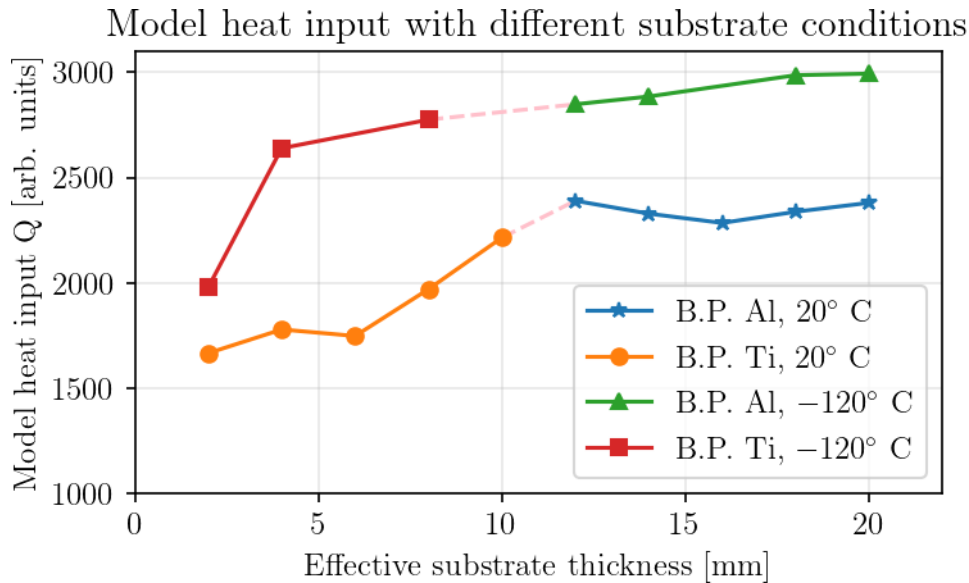


Figure 6.9: Model heat input vs substrate thickness for different substrate conditions.

Fig. 6.10 combines Figs. 6.4, 6.9 together, showing the relation between the deposition efficiency and the calculated model heat input for all investigated cases. The plot shows that for each substrate condition the deposition efficiency is an increasing function of the heat input. Additionally, after the outliers with lower efficiency values (plotted with empty markers on Fig. 6.10) are removed, the rest of the points form a linear trend over various substrate conditions. This leads to the conclusion, that in FS deposition there is a parameter window, where the deposition efficiency is a linear function of the amount of heat dissipated from the depositing rod.

Additionally, Fig. 6.10 shows that pre-cooling the substrate may not be the most effective way to increase the deposition efficiency. Consider the red and orange points that have similar heat inputs of  $\sim 2000$  a.u., but the efficiencies different by 15%. The two FS depositions show similar heat inputs, because one of them was on a

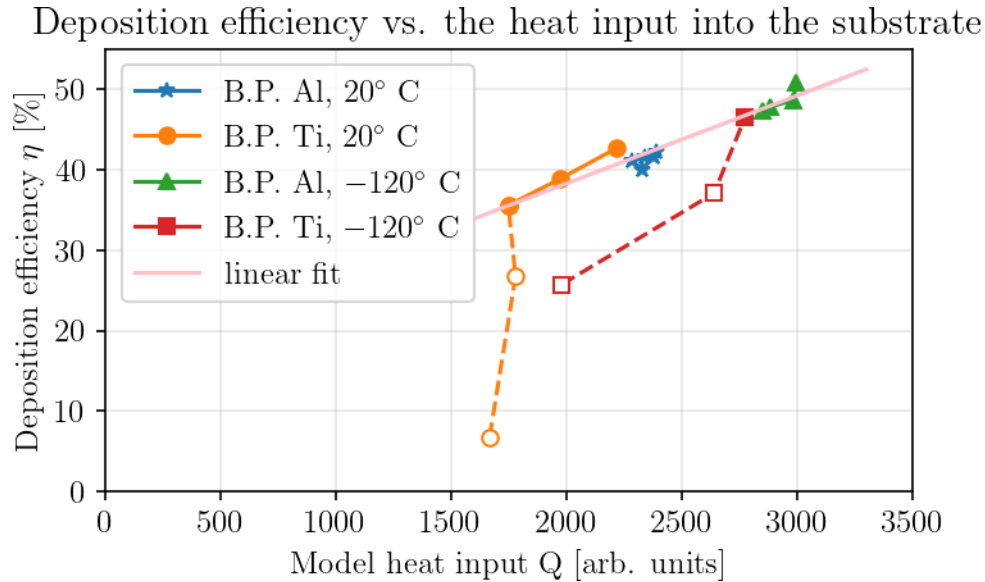


Figure 6.10: Deposition efficiency vs model heat input. Empty markers show the points not used in the linear fit. The estimated error in deposition efficiency is  $\delta\eta = \pm 4\%$ .

thicker substrate, and the other heated from a lower temperature. However, the lower temperature seems to be less preferable compared to thicker substrate, since the resulting efficiency is lower. Also, it is possible that this trend continues upwards, and an increased substrate temperature would yield a higher deposition efficiency at the same heat input compared to a thinner substrate. If it is so, then the most effective way to deposit FS coatings is on a pre-heated substrate with active cooling of the depositing rod. This requires further investigation.

**Comparison of different translational velocities** Depositions were performed on the 2 and 4 mm thick substrates with translational velocities 16 mm/s, 20 mm/s, 24 mm/s (see Table 6.2). Fig. 6.11 shows the model heat input vs. translational stud velocity relation. If the depositing rod was a constant power heater, the increase in heat input would have been proportional to the dwell time. But such a small increase in heat input (5% for 20 mm/s and 16% for 16 mm/s compared to 24 mm/s) can be explained by the heat generation being self balancing: the hotter the material gets, the less heat is generated by friction due to material's plastification. So even with the heat generator's dwell time being 33.3% longer, its heating power becomes smaller, so that during longer dwell time it produces a similar total amount of heat.

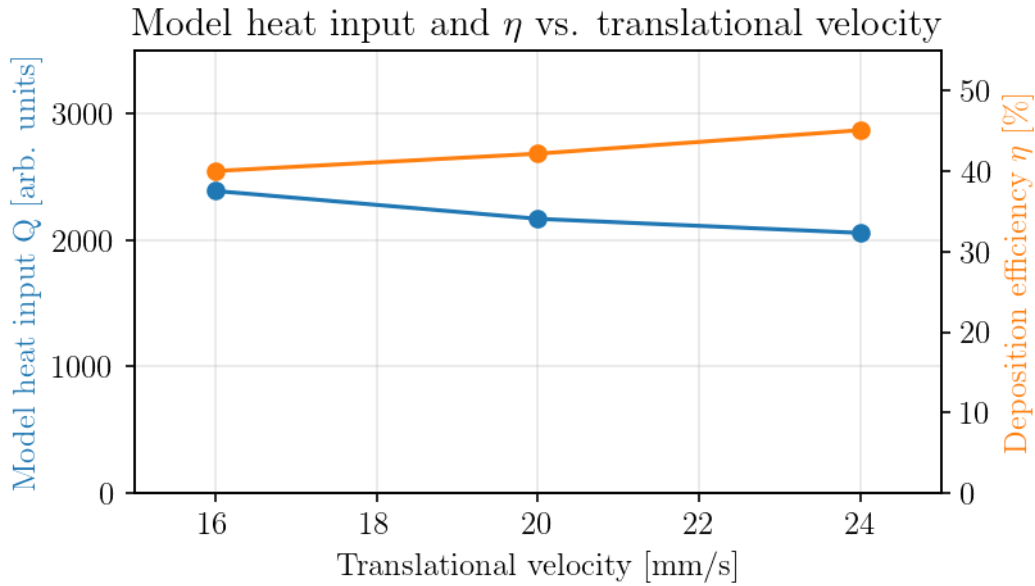


Figure 6.11: Heat input during AA6082 on AA2024 deposition for various translational velocities.

Fig. 6.11 also shows that when the heat input is slightly decreased by increasing the translational velocity, deposition efficiency slightly increases. This does not contradict the previous results, where the efficiency decreased with the heat input decrease. Translational velocity change makes a complicated case, since it affects both ends of the heat generation / dissipation balance. Also the observed changes in deposition efficiency are small relative to other investigated cases. This case requires further investigation, for example on thinner substrates with heat isolation, where the effect of the translational velocity change will be more clear.

**The heat input and the residual stresses** Calculated model heat input for the investigated sample sets explains the lack of diversity in the RS results from the previous chapter. Figs. 6.12, 6.13 6.14 repeat the results that are discussed in detail in Section 5.3.

Figs. 6.12, 6.13 show the residual stresses measured in transmission geometry for the AA6082 on AA2024 FS welds deposited with different translational velocities. Small changes in the RS state between the investigated samples correspond with small changes in both the amount of deposited material and heat input during the deposition (Fig. 6.11).

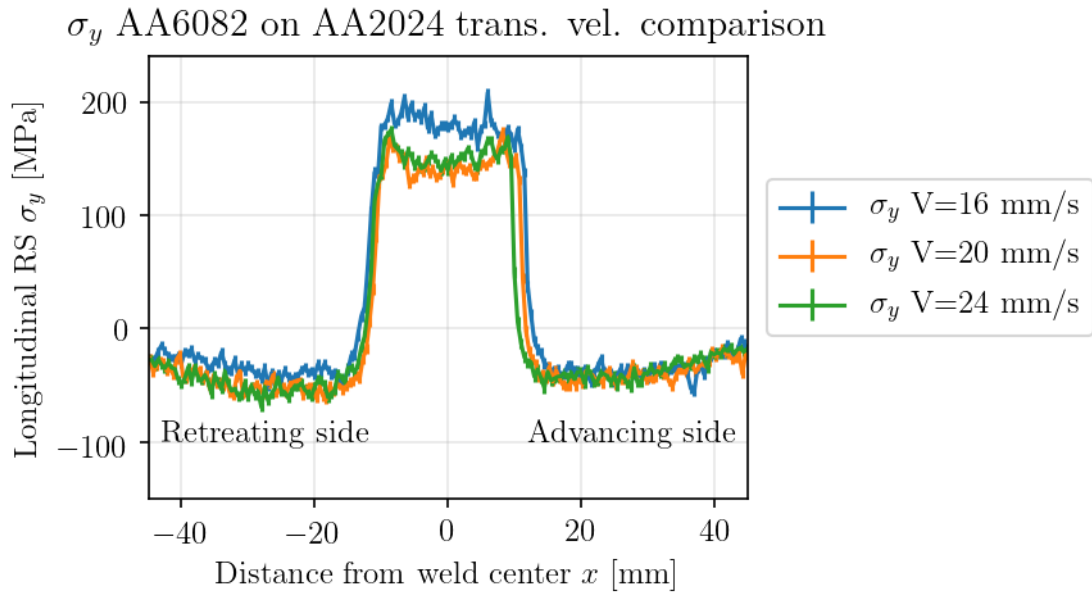


Figure 6.12: Longitudinal  $\sigma_y$  RS distribution along the scan line after coating deposition as determined from X-ray diffraction in transmission geometry.

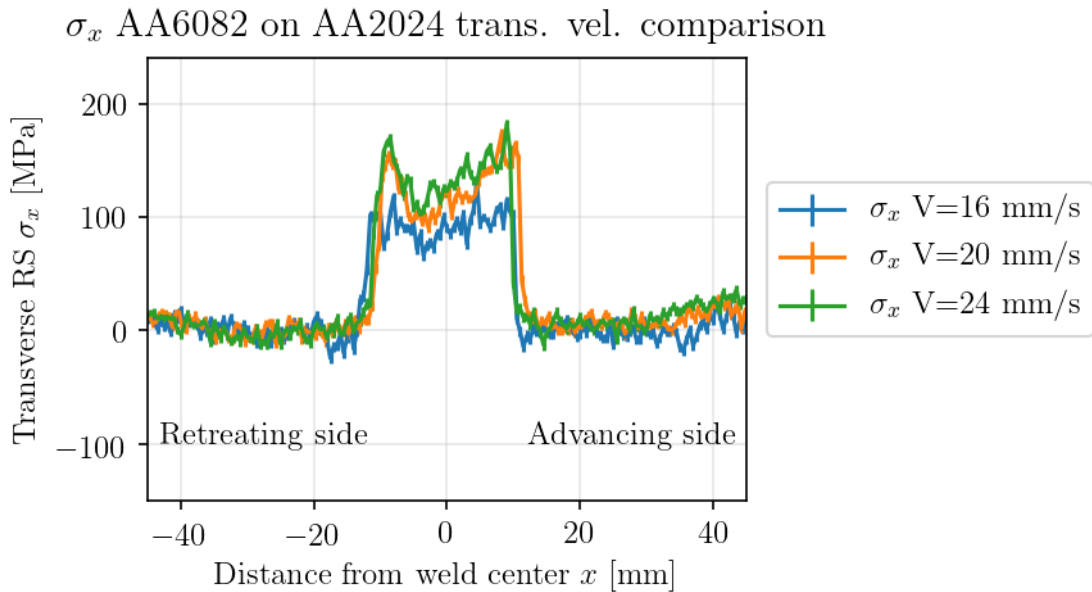


Figure 6.13: Transverse  $\sigma_x$  RS distribution along the scan line after coating deposition as determined from X-ray diffraction in transmission geometry.

Fig. 6.14 shows the residual stress states of the sheets of different thickness whose FS coatings were deposited with the same parameters. The RS in these sheets look so similar due to the fact that the thermal fields during the deposition were the same in all of them. This is shown by the blue line on Fig. 6.9 indicating similar heat input.

The only difference in the stress formation within this sample set is the position of the substrate edge making a mechanical cutoff, hence the stress fields looking like the same function cut off at different points.

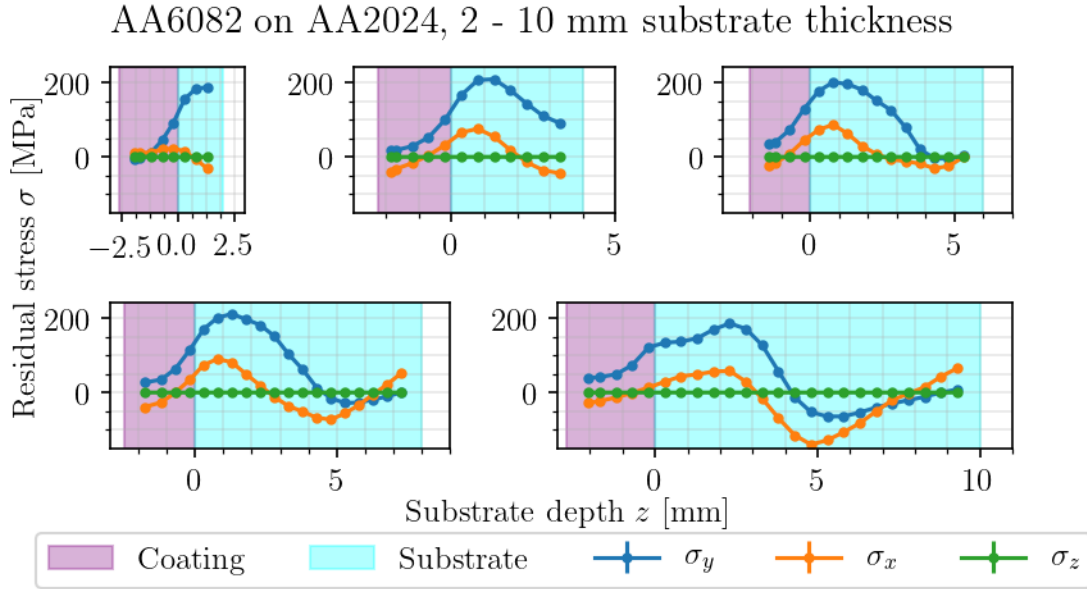


Figure 6.14: RS distributions as measured by neutron diffraction for different substrate sheet thicknesses.  $\sigma_z$  is 0 due to the plane stress condition. Mean error is  $\delta\sigma \simeq 10$  MPa, so the errorbars are not clearly visible.

## 6.4 Conclusions

1. When depositing AA6082 on AA2024 FS coatings, one has to take into account the substrate and backing plate heat conductivity. Deposition on 2 mm thick substrates requires a heat sink, which can be a 10 mm thick Al backing plate. Deposition on thicker substrates does not require a heat sink, but the deposition efficiency increases when it is utilised.
2. For AA6082 on AA2024 FS, cooling the substrate and the backing plate to  $-120^\circ\text{C}$  before the deposition yields an increase in efficiency of  $\sim 10\%$  compared to deposition at room temperature.
3. More generally, the deposition efficiency of FS increases when heat is dissipated from the depositing rod more effectively. Heat can be dissipated into the sub-

strate, as shown in this study or into the environment, as shown by [Li and Shinoda, 2013].

4. A decrease in the substrate temperature to  $-120^{\circ}\text{C}$  while keeping the heat dissipation constant leads to  $\sim 15\%$  deposition efficiency decrease. This suggests that the best efficiency would be achieved with the active cooling of the stud tip and pre-heating of the substrate. This requires experimental proof.
5. The small differences in RS between different translational velocities observed in the previous chapter can be explained by the small differences in heat inputs and working temperatures.
6. The RS formation in the Al substrate happens due to the material's thermal self equilibration, not air cooling, as this is the mechanism behind the rapid temperature decrease in the HAZ.

# Chapter 7

## Overall results and discussion

### 7.1 Residual stress characterization of Friction Surfacing

Coating deposition by Friction Surfacing was investigated for three coating-substrate material combinations: Ti-6Al-4V on Ti-6Al-4V, AA5083 on AA2024, and AA6082 on AA2024. Ti- and Al-based alloys were chosen, as they are significantly different in terms of the FS process parameters, and together make a good starting point for the process characterization. The Ti-6Al-4V alloy was chosen as one of the most common industrial Ti-based alloys. AA5083 and AA6082 were chosen as coating materials for AA2024, because such coatings could improve the corrosion resistance of the high-strength structural alloy AA2024.

Figure 7.1 shows the residual stress distributions for different translational velocities normalised to each material's yield stress. The plots show that there is a typical RS distribution for the Friction Surfacing process. The longitudinal ( $\sigma_y$ ) RS distribution is characterised by an active zone slightly wider than the deposited coating, with high tensile stresses, very steep gradients at the edges, and flat or M-shaped center. Around the active zone the compensative zone with compressive RS is formed to balance the tensile stresses. For Ti-6Al-4V the compensative zone of  $\sigma_y$  was shown to be able to retard and divert crack propagation. The same behaviour is expected from AA2024-based samples, but proving this requires further investigation.

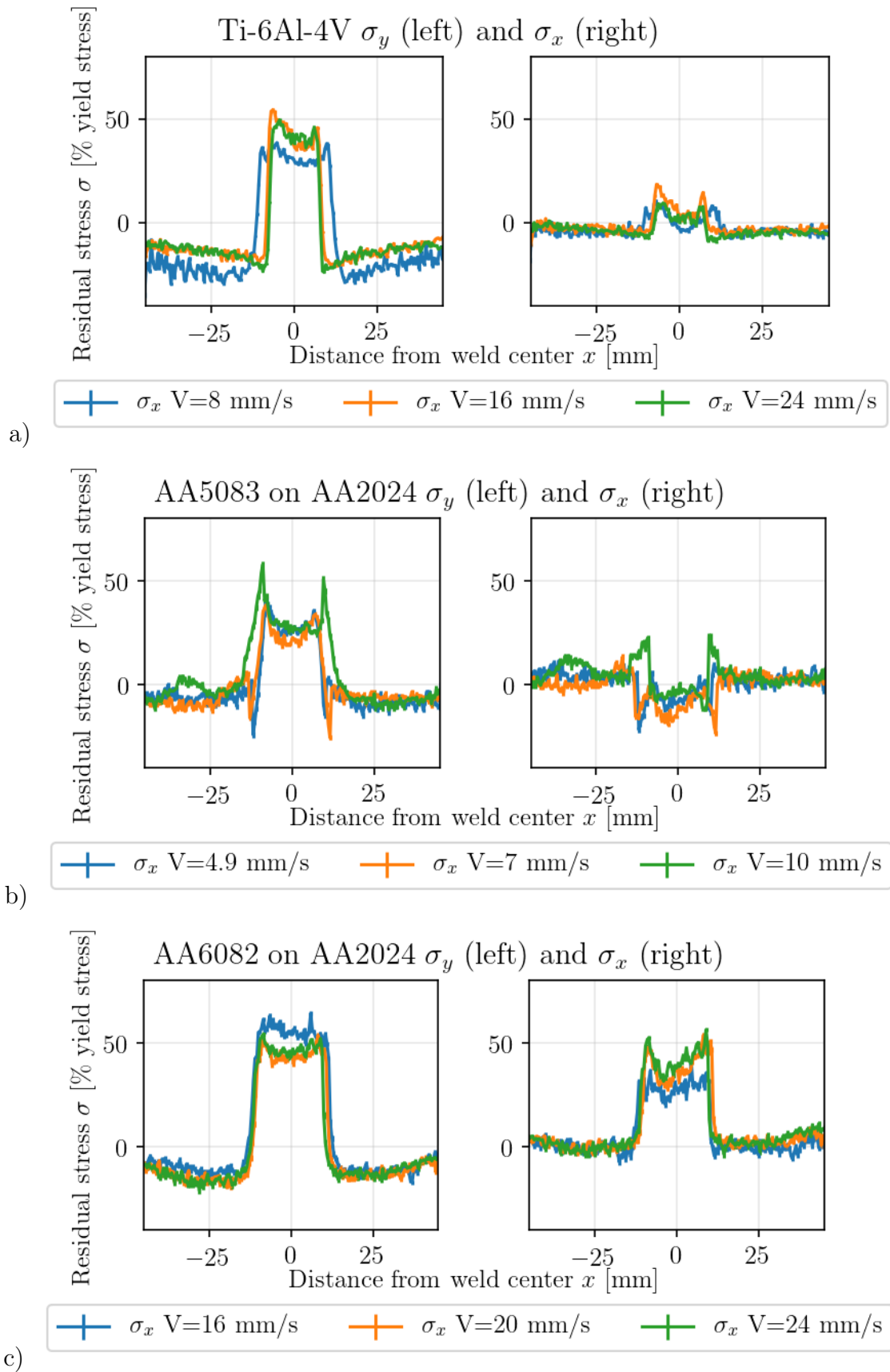


Figure 7.1: Residual stress distributions of investigated FS coatings normalised to the material's yield stress: a) Ti-6Al-4V on Ti-6Al-4V, b) AA5083 on AA2024, c) AA6082 on AA2024.

The transverse ( $\sigma_x$ ) RS distribution is similar in the Ti-6Al-4V and AA6082 FS coatings: the active zone is in a similar stress state in transverse and longitudinal directions, but has lower amplitude and more pronounced M-shape for  $\sigma_x$  compared to  $\sigma_y$ . The difference between the  $\sigma_x$  and  $\sigma_y$  projections is a consequence of the coating geometry: elongation of the heat affected zone in  $y$  direction leads to higher  $\sigma_y$  along the coated area. In AA5083 coatings the  $\sigma_x$  stress state is different, with negative values in the active zone. This might be a consequence of precipitation dissolution in AA2024 alloy and material softening, but a definitive answer requires further investigation.

For AA6082 on AA2024 FS deposited coatings most of the tensile stresses are formed in the substrate right below the coating. This behaviour is likely to be present in other materials as well, but proving this requires further investigation. The tensile stresses in the active zone are uniform along the deposition direction. For all investigated material combinations the residual stress state is independent from the axial force or stud consumption rate fluctuations during the deposition and is determined by the heat treatment of the substrate.

More details on the RS state of FS welds for each investigated material:

1. For Ti-6Al-4V coatings deposited at  $3000 \text{ min}^{-1}$  rotational speed,  $1.8 \text{ mm/s}$  stud consumption speed, and  $8-24 \text{ mm/s}$  translational speed, the heat input into the substrate material appears to be enough to form compact tensile stress zones (up to 44% yield stress) with very steep edges. However, at  $8 \text{ mm/s}$  translational speed, we see a decrease in the tensile stress values and also the broadening of the tensile stress zone. Both changes can be explained by the increase in heat input and more significant substrate plastification during the deposition.
2. AA5083 coatings on AA2024 substrate deposited at  $1500 \text{ min}^{-1}$  rotational speed,  $9 \text{ kN}$  axial force, and  $4.9-10 \text{ mm/s}$  translational speed, appear to show similar behaviour, with some detail changes. At lower translational velocities we also see a decrease in the tensile stress values, and the plastification of the substrate material appears to play a more significant role: the “relaxed” zone of the M-shape is wider compared to Ti-6Al-4V and the proportion of the highest to lowest stress in the M-shape is higher.

3. Although maximal tensile stresses in AA5083 coatings reach up to 58% yield stress, the surrounding compressive stresses do not look as pronounced as for Ti-6Al-4V. This is most likely due to the differences in the mechanical properties between AA2024 and Ti-6Al-4V, but part of the reason may be the pre-existing rolling stresses in the AA2024 sheets.
4. AA6082 coatings on AA2024 substrate deposited at  $2000 \text{ min}^{-1}$  rotational speed, 9 kN axial force, and 16 – 24 mm/s translational speed, show higher tensile stresses than AA5083 coatings (65% yield stress) and no M-shape, probably due to lesser heat input and less substrate plastification. AA6082 coatings show no differences in RS between translational velocities due to very similar process temperatures and cooling rates.
5. In AA6082 coatings on AA2024 substrate the tensile stresses form in the substrate right below the coating. The coating itself is mostly stress-free and machining it off after the deposition does not change the RS state. The compensative compressive stresses tend to form below the tensile if the substrate thickness allows it, and on the backside of the sheet around the coated area. The fact that there is more compressive RS on the opposite to the coating side of the sheet is important for using the process to design the RS state.

## 7.2 On the deposition efficiency of Friction Surfacing

The connection between heat dissipation and deposition efficiency has been investigated for AA6082 on AA2024 FS welds. Multiple depositions were performed at different temperature ranges, with temperature data collected from the bottoms of the substrates to avoid influencing the process. The temperature data was then used in a FEM model to estimate the heat input into the substrate for each deposition.

A connection between the FS deposition efficiency and the temperature regime during the coating deposition was found during this investigation. The experimental results are presented on Fig. 7.2 and show the following:

1. The deposition efficiency increases with the substrate thickness increase until it reaches a saturation value.
2. Cooling the substrate of any investigated thickness down to  $-120^{\circ}\text{C}$  before the deposition yields an efficiency increase of  $\sim 10\%$ .

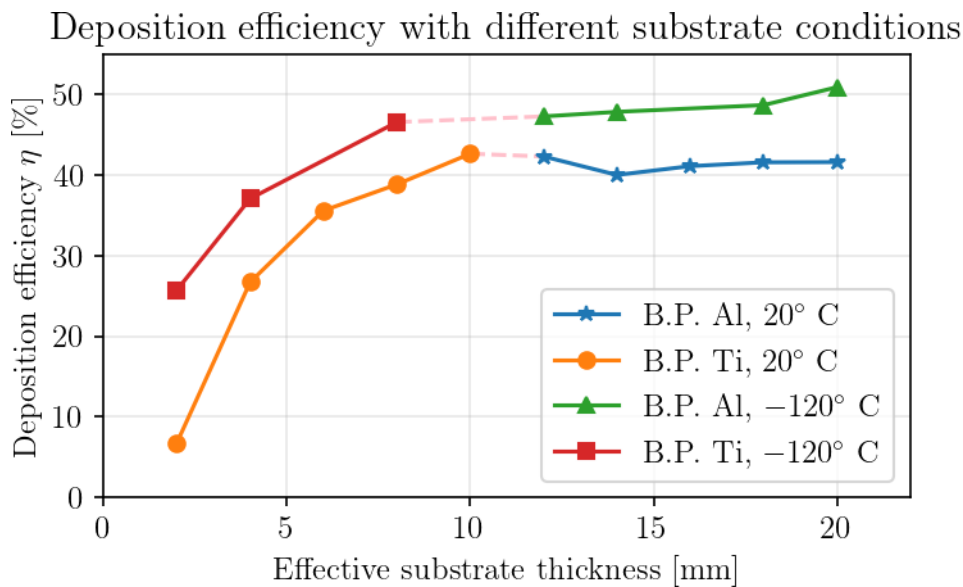


Figure 7.2: Deposition efficiency vs. substrate thickness for two starting temperatures:  $20^{\circ}\text{C}$  and  $-120^{\circ}\text{C}$ .

The experimental results put together with a 2D finite element heat propagation model have shown that the efficiency is an increasing function of the heat input into

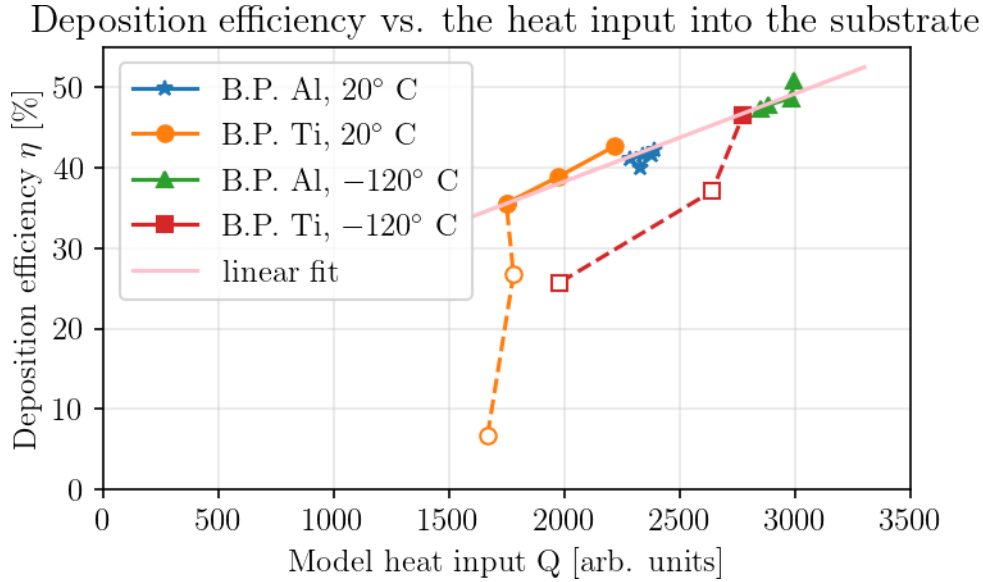


Figure 7.3: Deposition efficiency vs model heat input for various deposition conditions: Al or Ti backing plates (B.P.), liquid nitrogen (LN2) substrate pre-cooling or room temperature deposition. Empty markers are points not used in the fit.

the substrate during the rod dwell time (Fig. 7.3). For the sample sets where the heat dissipation properties are constant, such as pre-cooled and room temperature Al backing plate welds (blue and orange lines on Fig. 7.3), the change in the heat input is small, and so is the change in the deposition efficiency. For the pre-cooled and room temperature Ti backing plate sets (green and red lines on Fig. 7.3) the heat input increases with the substrate thickness, and so does the efficiency. The following conclusions can be made:

1. For FS a parameter window exists, where the deposition efficiency is a linear function of the heat input (see pink line on Fig. 7.3).
2. Improved heat dissipation from the depositing rod tip increases the deposition efficiency.
3. For materials with a high heat conductivity such as Al-based alloys not only the substrate geometry is important, but also the backing plate. Using heat conductive backing plates increases the deposition efficiency.

The results of this investigation make a very interesting starting point for multiple follow-ups:

1. Investigate the relationship between the heat input and the deposition efficiency for dissimilar welds, for example Al on steel, which has lower heat diffusivity. It may be that the efficiency depends on the substrate heat dissipation universally for all materials. Additionally, some material combinations might be incompatible due to poor substrate heat dissipation and can be made compatible with active or pre-deposition cooling.
2. Investigate if the efficiency is increased by:
  - (a) reducing the rotational velocity;
  - (b) active cooling of the stud tip;
  - (c) active cooling of the substrate bottom.
3. Investigate if the relationship between the heat input and the deposition efficiency holds for pre-heating the substrate.
4. Investigate if a combination of active cooling and pre-heating the substrate yields the best efficiency results, as the extrapolation of the current results would suggest.

### 7.3 On the scientific methods used in the study

Three types of stress-diffractometry experiments were performed in this study: in-transmission synchrotron diffraction, synchrotron diffraction with conical slits, angle-dispersive neutron diffraction. The experimental methods have proven their applicability and shown their limitations in the following ways:

1. In-transmission synchrotron RS measurements are a suitable way to estimate the stresses in  $\sim 2$  mm thick coatings on 2 mm thick sheets. However, there are significant stress gradients (up to 100 MPa/mm according to the neutron measurements) between the coating and the substrate, and at any specific point in-transmission measurements seem to show a random value from the gauge volume. For an in-transmission line scan of a 4 + mm thick sheet it adds up to significant noise.
2. For more than 2 mm thick sheets neutron diffraction can provide information on the depth distribution of the full stress tensor. However, for the exposure time to be reasonable the gauge volume can not be less than 0.5 mm for Al-based alloys and even larger for Ti-based alloys. Also gauge volume geometry does not allow to get information from points closer to the surface than 0.5 mm without special corrections that are impossible to implement for rough surfaces.
3. Synchrotron diffraction using conical slits complements the neutron measurements by providing less information (only two projections of the stress tensor with fixed gauge volume) at much lower exposure time, allowing to collect more data. This technique, while providing better resolution due to a smaller gauge volume, has the same limitation as neutron diffraction: collecting data from near the sample surface is complicated.
4. A good way to get more information on the RS distributions near the surface may be grazing incidence synchrotron diffraction. Although collecting data from the surface of the coating would be impossible without polishing, measuring the sample's backside could show if there is a compressive stress concentration there. However, this type of measurement was not performed in this study.

# Chapter 8

## Summary

Coating deposition by Friction Surfacing was investigated for three coating-substrate material combinations: Ti-6Al-4V on Ti-6Al-4V, AA5083 on AA2024, and AA6082 on AA2024. Ti- and Al-based alloys were chosen, as they are significantly different in terms of the FS process parameters, and together make a good starting point for the characterization of the residual stresses in the process.

An investigation into the residual stress state of FS coated sheets and its formation mechanism has shown that the stress state after the deposition is similar to other welding processes [Radaj, 2012], with a localized active zone of tensile stress and surrounding compensative zone of compressive stress. The stress state is strongly affected by changes in the translational velocity of the depositing rod for Ti-6Al-4V and only slightly affected by similar changes for Al-based alloys. The stress state is defined by the temperature regime during the deposition and is not affected by the axial force fluctuations. It is also not affected by machining the coating, which is a necessary element of post-production treatment. The experiments have shown that the residual stress state of FS coated sheets can be used for crack growth retardation. These results show good potential for FS to be used as a local modification process aimed at the increase of the fatigue life of the structural elements.

The heat input and the temperature regime during the deposition define not just the residual stress state, but the efficiency of the process and the amount of the deposited material. A combination of FS deposition experiments with finite element

heat propagation modelling have shown that for AA6082 on AA2024 FS welds increase of the heat dissipation from the depositing rod increases the amount of deposited material. This fundamental result has practical applications, such as necessity of a heat sink when depositing Al-based coatings on thin Al-based substrates, and gives a general insight into the process: at a certain parameter window efficiency of FS deposition is a linear function of the amount of heat the setup is able to dissipate from the rod.

The results obtained during this investigation can serve as a starting point for multiple follow-ups, both fundamental and applied. A natural continuation would be to see if the relationship between the heat input and the deposition efficiency can be extrapolated to dissimilar combinations by making a series of Al on steel or other depositions. Alternatively, one can apply the knowledge of the necessity for heat dissipation to dissimilar material combinations that have not been successfully joined to date, such as Al on Ti. Active cooling or adding heat sinks for Al on Ti depositions would solve the excess heat problem and potentially yield a successful joint.

For an extended investigation of the RS state a potential follow-up could be development of a FEM model of the stress formation during the process. Existing FEM models of FS published by [Liu et al., 2008], or [Pirhayati and Aval, 2019] focus on the material flow from the rod to the coating, which makes them powerful but complicated. Since the stresses in the coating and at the coating / substrate border are shown by this study to be relatively low, a useful approximation could be replacing the coating with a boundary condition and only computing the mechanical state of the substrate. That would simplify the calculation significantly and create a useful tool for stress state prediction based on the FS parameters and temperature measurements during the deposition.

# Acknowledgements

This work would not have been possible without the help and advice, both professional and personal, from many of my colleagues.

I would like to thank Dr. Peter Staron and Dr. Stefanie Hanke for their time, effort, expertise, and invaluable support.

I would like to thank Jonas Ehrich, Dr. Emad Maawad, and Dr. Weimin Gan for their help with the experimental work and fruitful discussions.

I would like to thank Prof. Dr. Sergei Grigoriev and Konstantin Pavlov, without whom I would not even have started a doctoral study.

Finally, I would like to thank Prof. Dr. Andreas Schreyer for the opportunity to work on this project and guidance.

# Bibliography

- [Allen et al., 1985] Allen, A., Hutchings, M., Windsor, C., and Andreani, C. (1985). Neutron diffraction methods for the study of residual stress fields. *Advances in Physics*, 34(4):445–473.
- [ASTM, 2008] ASTM, A. S. (2008). E647–05, 2005. *Standard test method for measurement of fatigue crack growth rates*. West Conshohocken (Pa): ASTM International.
- [Boyer and Gall, 1985] Boyer, H. E. and Gall, T. L. (1985). Metals handbook; desk edition.
- [Brewer et al., 2015] Brewer, L. N., Bennett, M. S., Baker, B., Payzant, E. A., and Sochalski-Kolbus, L. (2015). Characterization of residual stress as a function of friction stir welding parameters in oxide dispersion strengthened (ods) steel ma956. *Materials Science and Engineering: A*, 647:313–321.
- [Dovzhenko et al., 2018] Dovzhenko, G., Hanke, S., Staron, P., Maawad, E., Schreyer, A., and Horstmann, M. (2018). Residual stresses and fatigue crack growth in friction surfacing coated ti-6al-4v sheets. *Journal of Materials Processing Technology*, 262:104–110.
- [Edwards and Ramulu, 2015] Edwards, P. and Ramulu, M. (2015). Surface residual stresses in ti-6al-4v friction stir welds: pre-and post-thermal stress relief. *Journal of Materials Engineering and Performance*, 24(9):3263–3270.
- [Fitseva, 2016] Fitseva, V. (2016). *Friction Surfacing of Titanium Grade 1 and Ti-6Al-4V*. PhD thesis.
- [Fitseva et al., 2016] Fitseva, V., Hanke, S., dos Santos, J., Stemmer, P., and Gleising, B. (2016). The role of process temperature and rotational speed in the mi-

- crostructure evolution of Ti-6Al-4V friction surfacing coatings. *JMADE*, 110:112–123.
- [Fitseva et al., 2015] Fitseva, V., Krohn, H., Hanke, S., and dos Santos, J. (2015). Friction surfacing of Ti-6Al-4V: Process characteristics and deposition behaviour at various rotational speeds. *Surface & Coatings Technology*, 278(C):56–63.
- [Galvis et al., 2017] Galvis, J. C., Oliveira, P. H. F., Hupalo, M. F., Martins, J. P., and Carvalho, A. L. M. (2017). Influence of friction surfacing process parameters to deposit AA6351-T6 over AA5052-H32 using conventional milling machine. *Journal of Materials Processing Tech.*, 245:91–105.
- [Gandra et al., 2014] Gandra, J., Krohn, H., Miranda, R., Vilaça, P., Quintino, L., and Dos Santos, J. (2014). Friction surfacing—a review. *Journal of Materials Processing Technology*, 214(5):1062–1093.
- [Gandra et al., 2013] Gandra, J., Pereira, D., Miranda, R. M., and Vilaça, P. (2013). Influence of Process Parameters in the Friction Surfacing of AA 6082-T6 over AA 2024-T3. *Procedia CIRP*, 7:341–346.
- [Hanke and dos Santos, 2017] Hanke, S. and dos Santos, J. (2017). Comparative study of severe plastic deformation at elevated temperatures of two aluminium alloys during friction surfacing. *Journal of Materials Processing Tech.*, 247:257–267.
- [Hanke et al., 2017] Hanke, S., Staron, P., Fischer, T., Fitseva, V., dos Santos, J., and dos (2017). A method for the in-situ study of solid-state joining techniques using synchrotron radiation - observation of phase transformations in Ti-6Al-4V after friction surfacing. *Surface & Coatings Technology*, 335:1–45.
- [Hauk, 2010] Hauk, V. (2010). *Structural and Residual Stress Analysis by Nondestructive Methods*. Evaluation - Application - Assessment.
- [Hoyos et al., 2016] Hoyos, E., López, D., and Alvarez, H. (2016). A phenomenologically based material flow model for friction stir welding. *Materials & Design*, 111:321–330.

- [Hutchings et al., 2005] Hutchings, M. T., Withers, P. J., Holden, T. M., and Lorentzen, T. (2005). *Introduction to the characterization of residual stress by neutron diffraction*. CRC press.
- [John et al., 2003] John, R., Jata, K., and Sadananda, K. (2003). Residual stress effects on near-threshold fatigue crack growth in friction stir welds in aerospace alloys. *International Journal of fatigue*, 25(9-11):939–948.
- [Klopstock and Neelands, 1941] Klopstock, H. and Neelands, A. R. (1941). An improved method of joining or welding metals. Patent application No 572789.
- [Li and Shinoda, 2013] Li, J. Q. and Shinoda, T. (2013). Underwater friction surfacing. *Surface Engineering*, 16(1):31–35.
- [Liu et al., 2008] Liu, X., Zou, Z., Zhang, Y., Qu, S., and Wang, X. (2008). Transferring mechanism of the coating rod in friction surfacing. *Surface and Coatings Technology*, 202(9):1889–1894.
- [Lombard et al., 2009] Lombard, H., Hattingh, D., Steuwer, A., and James, M. (2009). Effect of process parameters on the residual stresses in aa5083-h321 friction stir welds. *Materials Science and Engineering: A*, 501(1-2):119–124.
- [Masubuchi, 2013] Masubuchi, K. (2013). *Analysis of welded structures: residual stresses, distortion, and their consequences*, volume 33. Elsevier.
- [McKinney, 2010] McKinney, W. (2010). Data structures for statistical computing in python. In van der Walt, S. and Millman, J., editors, *Proceedings of the 9th Python in Science Conference*, pages 51 – 56.
- [Muzvidziwa et al., 2016] Muzvidziwa, M., Okazaki, M., Suzuki, K., and Hirano, S. (2016). Role of microstructure on the fatigue crack propagation behavior of a friction stir welded ti-6al-4v. *Materials Science and Engineering: A*, 652:59–68.
- [Paris and Erdogan, 1963] Paris, P. and Erdogan, F. (1963). A critical analysis of crack propagation laws. *Journal of basic engineering*, 85(4):528–533.
- [Peel et al., 2003] Peel, M., Steuwer, A., Preuss, M., and Withers, P. (2003). Microstructure, mechanical properties and residual stresses as a function of welding speed in aluminium aa5083 friction stir welds. *Acta materialia*, 51(16):4791–4801.

- [Pirhayati and Aval, 2019] Pirhayati, P. and Aval, H. J. (2019). An investigation on thermo-mechanical and microstructural issues in friction surfacing of al-cu aluminum alloys. *Materials Research Express*, 6(5):056550.
- [Pouget and Reynolds, 2008] Pouget, G. and Reynolds, A. P. (2008). Residual stress and microstructure effects on fatigue crack growth in aa2050 friction stir welds. *International Journal of Fatigue*, 30(3):463–472.
- [Radaj, 2012] Radaj, D. (2012). *Heat effects of welding: temperature field, residual stress, distortion*. Springer Science & Business Media.
- [Rafi et al., 2011] Rafi, H. K., Phanikumar, G., and Rao, K. P. (2011). Material flow visualization during friction surfacing. *Metallurgical and Materials Transactions A*, 42(4):937–939.
- [Randau et al., 2011] Randau, C., Garbe, U., and Brokmeier, H. G. (2011). Stress-TextureCalculator: a software tool to extract texture, strain and microstructure information from area-detector measurements. *Journal of Applied Crystallography*, 44(3):641–646.
- [Romero et al., 2009] Romero, J., Attallah, M. M., Preuss, M., Karadge, M., and Bray, S. E. (2009). Effect of the forging pressure on the microstructure and residual stress development in Ti–6Al–4V linear friction welds. *Acta Materialia*, 57(18):5582–5592.
- [Sakihama et al., 2003] Sakihama, H., Tokisue, H., and Katoh, K. (2003). Mechanical Properties of Friction Surfaced 5052 Aluminum Alloy. *MATERIALS TRANSACTIONS*, 44(12):2688–2694.
- [Shi et al., 1990] Shi, Y., Chen, B., and Zhang, J. (1990). Effects of welding residual stresses on fatigue crack growth behaviour in butt welds of a pipeline steel. *Engineering fracture mechanics*, 36(6):893–902.
- [Staron et al., 2014] Staron, P., Fischer, T., Keckes, J., Schratte, S., Hatzenbichler, T., Schell, N., Müller, M., and Schreyer, A. (2014). Depth-Resolved Residual Stress Analysis with High-Energy Synchrotron X-Rays Using a Conical Slit Cell. *Materials Science Forum*, 768-769:72–75.

- [Steuwer et al., 2012] Steuwer, A., Hattingh, D., James, M., Singh, U., and Buslaps, T. (2012). Residual stresses, microstructure and tensile properties in ti-6al-4v friction stir welds. *Science and Technology of Welding and Joining*, 17(7):525–533.
- [Sun et al., 2017] Sun, T., Roy, M., Strong, D., Withers, P. J., and Prangnell, P. B. (2017). Comparison of residual stress distributions in conventional and stationary shoulder high-strength aluminum alloy friction stir welds. *Journal of Materials Processing Technology*, 242:92–100.
- [Toby and Von Dreele, 2013] Toby, B. H. and Von Dreele, R. B. (2013). Gsas-ii: the genesis of a modern open-source all purpose crystallography software package. *Journal of Applied Crystallography*, 46(2):544–549.
- [Tongne et al., 2017] Tongne, A., Desrayaud, C., Jahazi, M., and Feulvarch, E. (2017). On material flow in friction stir welded al alloys. *Journal of Materials Processing Technology*, 239:284–296.
- [Vilaca et al., 2012] Vilaca, P., Gandra, J., and Vidal, C. (2012). Linear Friction Based Processing Technologies for Aluminum Alloys: Surfacing, Stir Welding and Stir Channeling. In *Aluminium Alloys - New Trends in Fabrication and Applications*, pages 1–41. InTech.
- [Withers and Bhadeshia, 2001] Withers, P. J. and Bhadeshia, H. (2001). Residual stress. part 1—measurement techniques. *Materials science and Technology*, 17(4):355–365.
- [Wolfram Research Inc., 2018] Wolfram Research Inc. (2018). Mathematica, Version 11.3. Champaign, IL, 2018.